Reprint from the *Journal of Geophysical Research*, vol. 106, no. B11, pages 26,707-27,729, November 10, 2001.

Finite element models of stress orientations in well-developed strike-slip fault zones: Implications for the distribution of lower crustal strain

John C. Lynch and Mark A. Richards
Department of Earth and Planetary Science, University of California, Berkeley, California, USA

Abstract

Finite element models are used to examine the effects of strike-slip earthquakes on stresses in an elastic layer overlying a finite width viscoelastic shear zone in the lower crust. The overall dimensions of the model are 300 km wide, 400 km long, and 50 km deep. Three geometries for the lower crustal shear zone are considered: (1) a viscoelastic half-space approximation, with a shear zone that extends to the model boundaries (300 km in width); (2) a wide shear zone model (70 km in width); and (3) a narrow shear zone model (10 km in width). Earthquakes are simulated with a fault plane that slips without friction at the desired time step and is centered above the shear zone, extending to a depth of 15 km and running the length of the mesh. Far-field plate velocity boundary conditions are enforced at the model edges so that stress on the fault evolves naturally. A Coulomb-type failure criterion based on the average shear stress on the fault is set such that the earthquake cycle is $\sim$250 years. The models are run until a limit cycle is reached and transient stresses have decayed away. We focus on the maximum changes in the stress field during the earthquake cycle by examining stresses before and immediately after each earthquake. In addition to comparisons of the separate components of the stress tensor we present results in the form of maximum compressive stress orientations, plunge angles of the principal stress axes, and beach ball diagrams that facilitate visualizing the full tensor. Stresses are concentrated in the upper crust where it overlies the finite width viscoelastic shear zone, which causes the plunge angles of the principal stress axes to rotate from Andersonian orientations of 90° and 0° to angles that approach 45° in the lower crust. Our results suggest that an examination of stress orientations in the upper and middle crust from borehole breakouts and focal mechanisms may provide insight as to the distribution of strain in the lower crust and may eventually allow us to distinguish between localized and distributed deformation models for the lower crust in active strike-slip zones.

1. Introduction

The relationship between stress measurements in the upper crust and earthquake faults is poorly understood. Extrapolating from laboratory measurements of rock fracture mechanics to fault mechanics has proven to be difficult, and in the case of the San Andreas Fault in California, the two often appear incommensurate. Further, and not unrelated, a current debate in tectonophysics concerns the distribution of strain in the lower crust beneath continental strike-slip faults. While various lines of evidence have been used to suggest that deformation in the lower crust is broadly distributed about the San Andreas Fault, an unequivocal data set has yet to be found that rules out the possibility of highly localized strain in the deep crust. In this paper, we address both of these topics using finite element models of crustal stress near a strike-slip fault overlying a variable-width viscoelastic shear zone.

The primary observations that motivate this work are stress orientations in the crust. Throughout much of California, the maximum compressive stress (MCS), as determined from earthquake focal mechanisms and borehole breakouts, is nearly perpendicular to the San Andreas Fault (SAF) [*Zoback et al.,* 1987; *Mount and Suppe,* 1992; *Hardebeck and Hauksson,* 1999]. On a more local level, the MCS has also been observed to be nearly perpendicular to faults that experienced major earthquakes [*Zoback and Beroza,* 1993; *Hauksson,* 1994]. Classical models of faulting and static earthquake mechanics cannot explain these observations. *Anderson*'s [1951] theory of faulting, which is based on the Navier-Coulomb friction law, predicts that prior to an earthquake the orientation of the MCS should be in the range of 30°-45° with respect to the fault, corresponding to fault pore pressures that range from zero to the magnitude of the least compressive stress. Modifying this simple analysis by accounting for the smaller amount of shear stress necessary to reactivate preexisting fault structures, it can be shown that for a coefficient of friction of 0.6, the absolute maximum angle between the MCS and fault approaches 60° as the ratio of the maximum compressive stress to the minimum compressive stress approaches infinity [*Sibson and Xie,* 1998]. The orientation of the MCS in California would thus make thrust faulting seem more likely on the SAF than strike slip. Yet the history of seismicity in California over the last 150 years shows that $> 90\%$ of the moment released has been pure strike slip [*Bakun,* 1999; *Ellsworth,* 1990]. Further, while there has been success with modeling some types of fault movements (e.g., afterslip, stick-slip, creep) using more modern "rate and state" friction laws, the orientation of major strike-slip faults in California with respect to principal stresses is still difficult to explain.

The apparent misorientation of stress with respect to major faults can be described as an observation in need of an explanation. On the other hand, current ideas about the distribution of strain in the lower crust are examples of conjecture in need of discriminating observations. In other words, even less is known about the nature of the deformation that takes place below the seismogenic zone. Very few earthquakes nucleate below depths of 15-20 km in California, but the relative motion of the faults must be accommodated in some aseismic fashion below this depth in the lithosphere. Hints as to the characteristics of this motion come from deformation recorded at the surface, often in the form of postseismic strain. To model these observations, two archetypal approaches have been widely used and their relative merits debated. In the first conceptual model, continental faults cut the entire lithosphere, with some form of continuous slip occurring on the fault below the seismogenic zone [*Savage and Burford,* 1970; *Thatcher,* 1983]. In the second, continental faults cut only to the seismogenic depth, and ductile deformation accommodates intraplate strain below the fault in a broadly distributed manner [*Nur and Mavko,* 1974; *Prescott and Nur,* 1981; *Thatcher,* 1983]. The results from these models are then compared to geodetic data, or alternatively, geodetic data are used to find an acceptable model using an inverse method. These approaches have proved to be very useful in California [e.g., *Thatcher,* 1983; *Lisowski et al.,* 1991]. However, *Savage* [1990] pointed out that conclusions drawn from these models are entirely ambiguous with regards to the mechanism for postseismic strain, and he showed that the two approaches can give equivalent (indistinguishable) results at the surface for models with faults of infinite length.

Another data set that may prove useful in this debate comes from a recently developed method for examining the stress regime near faults that makes use of the effect of the Earth's surface on stress orientations [*Bokelmann and Beroza,* 2000]. Like the studies of the maximum compressive stress orientation, this method uses earthquake focal mechanisms to infer stress. However, the stress-free boundary condition at the Earth's surface, where shear stresses in the horizontal plane must be zero, is also used as a guide to

understand the orientation of the stress tensor. The plunge angles for the pressure, null, and tension (P, B, and T) axes, determined from focal mechanisms, are examined, and it is found that their orientations are aligned with the principal stresses near the free surface, one of which must be perpendicular and the other two coplanar with the horizontal plane. Additionally, Bokelmann and Beroza use a proxy for the horizontal shear stress derived from the off-diagonal elements of the moment tensor and show that this varies from the lowest values at the free surface to a maximum at a depth of 5 to 9 km and then to lower values again at depths greater than this. They interpret this observation as an indication of a nearly traction-free surface in the lower crust due to a weak zone below that.

All of these data, along with previously used modeling techniques, have guided the development of our models. The majority of computational models of crustal deformation due to major strike slip faults in the past have been either analytical and focused on surface deformation and velocity/strain fields [*Nur and Mavko,* 1974; *Thatcher,* 1983; *Savage and Prescott,* 1978; *Cohen,* 1982; *Savage,* 1990; *Pollitz and Sacks,* 1992] or numerical and focused on particular components of the stress tensor within a cross section of the crust [*Lyzenga et al.,* 1991; *Verdonck and Furlong,* 1992]. Both types of models are two-dimensional (2-D) and assume an infinitely long fault, as well as one of the previously mentioned mechanisms for relaxation of the crust beneath the brittle-ductile transition zone. Our goal has been to build on these models while keeping the overall conceptual ideas as simple as possible. Like the previous numerical models, we focus on the evolution of stress in time near a periodically slipping fault. We use a 3-D finite element method but maintain a 2-D approximation by considering a fault that is much longer than its depth. Material models are linear elastic and linear viscoelastic, and the lower crustal shear zone is purposefully made without geometric complexity. Unlike previous models, however, we examine the effects of ductile flow being broadly distributed beneath strike-slip faults versus being highly localized by prescribing viscoelastic shear zones of various widths. The primary result here is that the orientation of the principal stresses in the upper crust may give some clues as to the style of deformation in the lower crust.

2. Methods

2.1. Model Description

The finite element mesh used for the present study represents a domain 300 km in width, 400 km in length, and 50 km deep, and consists of over 7000 elements (Plate 1). To model the fault, the mesh is split lengthwise at the center to a depth of 16 km, and the element faces on either side of the cut are defined as contact elements (described in section 2.2). Directly beneath the fault, a linear viscoelastic shear zone is prescribed from a depth of 15 to 50 km. One result of this geometry is that the fault tip, or bottom of the fault, is beneath the elastic-viscoelastic transition, which allows for diffusion of the large coseismic stresses concentrated there, rather than a buildup from one earthquake to the next. In order to model the effects of strain localization in the lower crust the viscoelastic shear zone was varied in width for each of the three models presented here: 300 km (half-space approximation), 70 km (wide shear zone), and 10 km (narrow shear zone). Plate 1 shows the wide shear zone mesh (case 2).

Plate 1

The general purpose, commercial 3-D finite element package Spectrum™, developed by Centric Engineering Systems, Inc. (recently acquired by Ansys, Inc.), was used to model repeating earthquakes on a strike-slip fault. As we used linear material models, standard finite element techniques were sufficient for the solution [see, e. g., *Hughes,* 1987; *Zienkiewicz and Taylor,* 1991]. The exception to this is at the fault plane itself, where it was necessary to develop a special contact element and a fault failure mechanism.

2.2. Fault Characteristics

In general, finite element contact problems, a portion of the boundaries of two contacting bodies are defined as the contact surfaces and are monitored for potential interaction. In our case, the contacting bodies are the two sides of the fault, which become one continuous body at a depth of 16 km (i.e., at 15 km and above, nodes are defined as part of contact surfaces for either side of the fault, and at 16 km and below, the two halves of the mesh share their nodes and are therefore continuous). Conventionally, one of the surfaces is defined as the master contact surface, and the other as the slave contact surface. Contact is determined by the penetration of the master surface by any of the nodes on the slave surface. Once penetration is detected, constraints are enforced at the contacting slave nodes (generally by a penalty or

augmented Lagrangian method) and this effectively creates the desired type of surface-surface interaction: free-slip (penetration constraint only), no-slip (penetration and sliding constraints), or slip with some type of friction law (penetration and modulated sliding constraints) (for a review of static contact theory in the finite element method, see *Zhong and Mackerle* [1992]).

In our models we required a fault (the contact surfaces) to be in free-slip mode during earthquakes and no-slip mode during the interseismic period and, additionally, a way for the solver to decide when to switch from one mode to the other via a failure criterion. The result was coined the "velcro" element, essentially a combination free-slip/no-slip element with a simple boolean flag to determine which constraints to enforce at any given time step. The velcro element also uses a "both sides master" or standard two-pass formulation, such that the penalty constraints are enforced identically on both surfaces. This is necessary in order to achieve results that are symmetric about the fault.

To set the constraint flag to one mode or the other, an approximation of the average shear stress on the fault is considered. During the interseismic period the penalty method is used to constrain the slave nodes to prevent both penetration and slip tangential to the surface. The penalty method can be thought of as constraining a nodal point by means of a spring, the spring constant of which is the penalty factor. As the penalty factor is increased, the constraint is enforced more accurately, but it is never enforced perfectly. The small displacements of the nodes in the penalized direction (of the order of 10^{-5} m for the models presented here) multiplied by the penalty factor can be thought of as a force or traction on those nodes or contact surface. The portion of the force that is tangential to the fault surface can then be considered as a proxy for the shear stress on the fault for the purposes of a Coulomb-like failure criterion [e.g., *Ju and Taylor,* 1988]. The average of these tangential forces is monitored at each time step, and once the average exceeds a predetermined threshold value, the flag is switched from no-slip to free-slip for one time step. Modeling the fault in this manner leads to almost complete stress drop (zero shear stress on the fault) for each earthquake.

The fault failure criterion was chosen such that an earthquake repeat time of roughly 250 years was achieved once the model had reached its limit cycle (discussed in section 3.1), which is of the same order as estimates for the repeat time for great earthquakes on the San Andreas Fault. Since the failure criterion is based on a proxy for the average shear stress, the actual threshold value is meaningless; however, the threshold corresponds to the fault failing when the average shear stress on the fault is $\sim$13 MPa. Alternatively, an algorithm could have been used that would cause the fault to fail with a specific repeat time (e.g., 250 years), though this would preclude the model from developing a natural limit cycle.

2.3. Model Inputs

We solve the linear momentum equation in time as a quasi-static problem and subject to the model inputs of material models (constitutive laws), boundary conditions, and a fault failure criterion. Inertial effects and the dynamics of fault rupture are ignored, as are gravitational (body) forces. The model consists of linear elastic and linear viscoelastic elements, with material parameters E (the Young's modulus) and ν (the Poisson's ratio) defined as 75 GPa and 0.25, respectively, for the entire mesh, and η (the Newtonian viscosity) defined as 10^{19} Pa s from a depth of 21 to 50 km within the shear zone only. A rough viscoelastic "transition zone" is defined between the elastic upper crust and the low-viscosity shear zone, such that $\eta = 10^{20}$ Pa s between the depths of 15 and 18 km, and $\eta = 3.16\times10^{19}$ Pa s between the depths of 18 and 21 km. We found that without such a transition zone the solution near the fault was unstable, leading to convergence problems. Additionally, this is a more physically reasonable rheological model for the brittle-ductile transition zone, though still very simple. The viscosity in the lower part of the shear zone corresponds to a Maxwell relaxation time of $\tau = \eta/E = 4.23$ years. We ran models with higher and lower values for the viscosity but found that as long as τ was at least an order of magnitude less than the earthquake repeat time ($\sim$250 years), the solutions were indistinguishable in the time steps immediately before and after the slip event time step itself. Changing the shear zone viscosity only changes the rate at which the upper crust is reloaded by the relaxing lower crust during the postseismic period, since for all viscosities considered (10^{18} Pa s $\leq \eta \leq 10^{20}$ Pa s, corresponding to 0.423 years $\leq \tau \leq$ 42.3 years), τ is such that the shear zone will be completely (or very nearly) relaxed before each slip event. Additionally, we model slip events such that they occur in time increments 2 orders of magnitude smaller than τ, and thus all models are behaving elastically for that time

step. As we are primarily concerned with the results at these time steps for the present study, we show results only for the vertical viscosity structure described above.

A constant velocity boundary condition is enforced on each of the two mesh faces parallel to the fault, for a total of 3.2 cm/yr of fault parallel displacement, which is comparable to the San Andreas Fault in northern California [*Lisowski et al.,* 1991]. The remaining boundaries (top, bottom, and ends) are defined as zero traction or free surfaces. The only other input to the model is the fault failure criterion (discussed in section 2.2).

2.4. Model Resolution

Element dimensions vary as a function of distance from the fault, where the gradients of displacement and stress are steepest. As we are using eight-node, linear hexahedral elements (with eight interior Gaussian integration points), it is crucial to concentrate elements in the regions where the solution is changing rapidly (in space and in time) in order to resolve those gradients. Using a mesh generator created by the MacNeal-Schwendler Corporation, MSC/PATRAN, we developed a mesh with elements that are 1.5 km by 1.25 km in the down dip (z) and fault perpendicular (x) directions at the fault and elements that are 3.75 km by 38.4 km at the mesh boundary, with a smooth transition between the two regions. After performing several tests (see Appendix A), we felt confident that elements of this size would resolve the stress gradients near the fault sufficiently to comment on the applicable data.

Along the strike of the fault (the y direction), the solution changes very little; in fact, for all practical purposes, the formulation here is a 2.5-D model, and we present the bulk of our results as cross sections through the center of the mesh (Plate 1). At the mesh boundaries where the fault ends, however, edge effects dominate the solution. Therefore we concentrate elements in that region so as to leave the center of the mesh uncontaminated by these errors at the ends of the mesh. This is achieved by defining elements that are 15 km in length at the edges and that smoothly grow to 45 km in length at the center. Examining the contours of fault parallel shear stress in Plate 1, we can see that inside of four elements from this boundary the solution is almost unchanging in the y direction.

Just as it is necessary to increase the mesh resolution near the fault, it is important to increase the time resolution immediately following a slip event (the postseismic period) for similar reasons. If the time increment chosen is too large, it is possible to underestimate the amount of strain energy that is transferred from the viscoelastic lower crust to the elastic upper crust and thereby to underestimate the loading of the fault early in the earthquake cycle. This is a result of the finite element solver making a linear approximation of the exponential relaxation of the Maxwell solid over the time step. Therefore it is necessary for the time increment, Δt, to be much less than τ. However, once several relaxation times have passed and the lower crust is relaxed, reloading of the fault reflects the constant velocity boundary conditions only and is therefore linear in time. During this interseismic period it is computationally expensive and unnecessary to use such a small time increment. For this reason, we forced the solver to take very small time increments during the postseismic period ($\Delta t =$ 0.01 years) and then allowed the time increments to slowly increase to 10.0 years over the next 40 model years (almost 10 relaxation times) for each earthquake cycle.

3. Results

3.1. Surface Displacements and Velocities

The models were run until both earthquake repeat times and shear stress magnitudes were roughly the same for each earthquake cycle. This limit cycle is reached once the transient effects due to the initial, unstressed condition of the viscoelastic material have had sufficient time to decay away. Larger viscoelastic shear zones require more time to reach the limit cycle than smaller shear zones. Figure 1 shows the displacement of four surface nodes at 0, 5, 35, and 150 km from the fault versus time for the half-space approximation model. The initial quiescent period, when stress is building up to the first earthquake, is not shown. The displacement curves indicate three zones of surface deformation: the node at the boundary has a constant velocity (reflecting the boundary condition enforced there); the node on the fault shows the stair-stepping pattern associated with its stick-slip behavior; and the nodes in between these two extremes show both coseismic and postseismic deformation effects. This case took the longest to reach the limit cycle, as evidenced by the long-period transient that affects both the coseismic displacement and the earthquake repeat time for roughly 6000 model years, starting at the onset of slip events (Figure 1).

This is not unlike the behavior seen by *Lyzenga et al.* [1991], and is a reflection of the time required for diffusive stress propagation throughout the viscoelastic domain.

The half-space approximation model that we present here is so named because of its similarity to analytic models of strike-slip faulting in an elastic layer over a viscoelastic half-space [*Nur and Mavko,* 1974; *Savage and Prescott,* 1978; *Savage,* 1990]. As an example of the type of results achieved with such models, in Figure 2 we show the surface velocity as a function of distance from the fault at various times in a mature earthquake cycle for our half-space approximation model. Except that it represents a mature fault zone, or limit cycle, the velocity field is similar to analytical results [e.g., *Savage,* 1990, Figure 2], and we therefore borrow the notation of those models: x is the distance from the fault, H is the fault depth, v is the local velocity, V is the far field velocity, and T is the earthquake repeat time. Holding other parameters constant, we find that the maximum postseismic velocity is inversely proportional to the Maxwell viscosity and to the width of the lower crustal shear zone. The overall shape of the velocity curves and the distance at which the maximum velocity is seen is dependent only on the depth of the fault. Thus a given velocity field can be reproduced with any number of shear zone width and viscosity structure combinations, rendering geodetic data unable to distinguish among such models. This result is similar to the ambiguity pointed out by *Savage* [1990] and *Zatman* [2000], in that the velocity profile at the surface is unrelated and decoupled from the velocity profile below the seismogenic layer for models with infinitely long faults. For this reason, we concentrate the bulk of this paper instead on modeled deviatoric stresses.

3.2. Shear Stresses Before and After Earthquakes

Plates 2 and 3 show contours of deviatoric shear stress through cross sections in the middle of the mesh for the three cases. For the σ_{xy} plot, all three cases exhibit the same stress magnitudes on the fault. Before the earthquake the deviatoric shear stress decreases from well over 25 MPa at the base of the fault to < 7.5 MPa at the surface. After the earthquake, shear stress is close to 0 MPa for the upper 13.5 km of the fault. Shear stress does not drop to exactly zero at the base of the fault due to the inaccuracies of the finite element approximation (see Appendix A). The viscoelastic shear zone beneath the fault is completely relaxed ($\sigma_{xy} = 0$ MPa) just before the earthquake and reacts elastically immediately after the earthquake. This gives rise to a stress concentration at the fault tip, with values of $\sigma_{xy} > 20$ MPa. In the elastic upper crust away from the fault the shear stress is relatively constant with depth, with values of 15-20 MPa above the shear zone in all three cases, and 2.5-5.0 MPa far from the shear zone in the finite width shear zone models (cases 2 and 3). A small concentration of shear stress can be seen in the finite width shear zone models just above the "corners" of the viscoelastic shear zone (especially in case 2), which is the result of the arbitrarily sharp material model transition at the shear zone boundary.

Basal shear stress (σ_{yz}, Plate 3) is concentrated at the interface between the two material models near the fault. It is equal and opposite in sign on either side of the fault, reflecting the equal and opposite deformation. The magnitude of the basal shear stress is of the same order as that of the fault parallel shear stress in the same region. Away from the fault tip, σ_{yz} is negligible.

3.3. Normal Stresses

Since only fault-parallel motion is enforced in our model, σ_{xy} and σ_{yz} are at least an order of magnitude larger than the other components of the stress tensor. Further, outside of a 5 km radius of the fault tip, σ_{xy} is the only significant component. Therefore, when the principal stresses are examined, one finds the maximum compressive stress oriented at close to 45° to the fault everywhere in the mesh and dipping strongly near the fault tip. In California, observations from boreholes and focal mechanisms show that the maximum compressive stress is nearly perpendicular to the San Andreas Fault, especially at distances greater than a few tens of kilometers [*Zoback et al.,* 1987; *Mount and Suppe,* 1992; *Hardebeck and Hauksson,* 1999]. Anderson faulting theory predicts that the orientation of the maximum compressive stress would range from 30° to 45°, depending on the amount of pore pressure, or perhaps as high as 60° for preexisting faults [*Sibson and Xie,* 1998]. Given these ranges for the orientation of the maximum compressive stress in observation and in theory, we superposed a simple normal stress calculation onto our shear stress calculations.

Normal stresses for the three cases were calculated by imposing a displacement that is normal to the fault at the edges of the mesh that are parallel to

the fault (the same edges on which the constant velocity boundary conditions are imposed for the shear stress calculations). The amount of displacement was chosen such that the resultant normal stress on the fault would be 20 MPa for the half-space approximation model, and then this value was used for all three cases. We chose 20 MPa because this is the minimum addition that would start to bring the orientation of the maximum compressive stress in our calculations in line with observations in California. We will discuss the effect of choosing a larger displacement in section 3.4. The depth-averaged shear stress on the fault at failure is ~ 13 MPa, so that if the lithostatic pressure were considered, the Coulomb friction coefficient would be < 0.10, putting our model in the "weak fault" category. However, this is a direct result of a fault that experiences a complete stress drop with each earthquake and is not affected by the amount or manner in which the stress normal to the fault is calculated. The amount of normal stress added (within this order of magnitude), then, is arbitrary, but choosing a smaller or larger displacement in our calculation would only change the magnitude of the normal stress, and not the overall pattern of stress distribution. Therefore, for all other case 1 results presented below, the post hoc 20-MPa normal stress has been added, independent of time. In addition to the enforced displacement the top and bottom boundaries have a zero displacement boundary condition in the vertical (z) direction. This causes the mesh to bulge slightly at the ends due to the Poisson effect but leads to a constant normal stress across the cross section of the half-space approximation model (Plate 4, case 1).

Cases 2 and 3 do not have a constant normal stress in space due to the finite width shear zones (Plate 4, cases 2 and 3). We assume that the normal stresses remain relatively constant throughout the strike-slip earthquake cycle and therefore have no time dependence. We also assume that the timescale over which these normal stresses are relevant is much longer than the duration of the earthquake cycle and several orders of magnitude larger than the Maxwell relaxation time for the viscoelastic shear zone. We therefore define the normal stress in the shear zone to be zero, which is equivalent to assuming that all normal stresses would be completely relaxed over the evolution of the strike-slip shear zone. This results in a concentration of normal stress above the shear zones in cases 2 and 3 that is similar to the concentration seen in the shear stress contours in Plate 3 for the same cases. These time-independent stress calculations are superposed on our shear stress calculations for cases 2 and 3 for all results reported below.

3.4. Maximum Compressive Stress Orientations in the Upper Crust

Figure 3 shows the orientation of the maximum compressive stress (MCS) with respect to the fault plane as a function of distance from the fault for the three cases. The superposition of the normal stress calculation causes the orientation of the MCS to lie between 60° and 90° with respect to the fault plane, as opposed to the uniform 45° that would be seen without the additional normal stress. This range of values is similar to the range of values seen for the orientation of the MCS with respect to the San Andreas Fault throughout California, lending some justification to our chosen amount of normal stress added.

The orientation of the MCS for both depths is roughly the same for all three models at the fault: between 70° and 77° before the earthquake and very close to 90° after the earthquake. These high angles drop off precipitously away from the fault zone, indicative of the higher shear stresses in the nearby crust. In the case of the half-space approximation model (case 1) the MCS is oriented at ~63° with respect to the fault plane at all points away from the fault due to the uniform level of shear and normal stress there. Cases 2 and 3 both exhibit a local minimum in the MCS at the point in the elastic crust that overlies the boundary of the viscoelastic shear zone: 35 km from the fault for case 2, and 5 km from the fault for case 3 (more clearly seen in the preearthquake trace for case 3). A local maximum in the MCS can also be seen for these cases at ~60 km from the fault for case 2 and ~25 km from the fault for case 3, though the locations of the maxima are less certain due to the decrease in mesh resolution at distances > 35 km from the fault (see Plate 1). The MCS then decreases to ~61° at the mesh boundary for case 2 and ~65° for case 3.

Were we to have chosen a larger normal stress to be added to these models, the effect would be to translate all of the curves toward higher angles of orientation with respect to the fault and toward smaller angles had we chosen less normal stress. Figure 4 shows the orientation of the maximum compressive stress for the wide shear zone model before an earthquake for three different amounts of normal stress added: 20 MPa (which is shown in Figure 3), 40 MPa and 60 MPa. Like Figure 3, 0 and 7.5 km depths are shown with

solid and dashed lines, respectively, but in Figure 4, only the preearthquake results are shown. As the normal stress component begins to dominate the MCS, the curves tend more toward an orientation perpendicular to the fault and the range of values decreases. For example, with 20 MPa of normal stress added, the orientations range from 60° to 75°, whereas with 60 MPa added the MCS ranges from 75° to 85°, with 5° less variation. The limit would be reached with an infinite amount of normal stress added, and the MCS would be 90° to the fault everywhere.

3.5. Evolution of the Maximum Compressive Stress Orientations

As an example of the time-dependent behavior of the stresses in our calculations, we show in Figure 5 the orientation of the maximum compressive stress at the fault for the half-space approximation model (case 1) as a function of time normalized by the length of the earthquake cycle. The low-viscosity shear zone causes the stress regime on the fault to change rapidly following an earthquake. This is especially true for the 7.5 km depth time history, where the maximum compressive stress angle goes from 90° with respect to the fault plane immediately after an earthquake to almost 75° after only 20% of the earthquake repeat time. Results for the other two cases are similar, and while the narrow shear zone model (case 3) reloads the fault more slowly in the early part of the cycle and nearly linearly in time, the beginning and ending orientations are nearly identical to case 1.

3.6. Plunge Angles of the Principal Stress Axes

In Figure 6 we show the plunge angles for the three principal stress axes as a function of distance from the fault for each of the three cases and at three depths. All plots are shown for the time step immediately before a slip event. The plunge is measured as the angle between the given axis and its projection into the horizontal plane and therefore varies from 0° to 90°.

As with the orientation of the maximum compressive stress, the three model cases yield similar results at the fault itself, while variations in the models can be seen in the surrounding crust. The maximum compressive stress axis remains in the horizontal plane for much of the model domain, with the exception occurring at the fault near the shear zone boundary, where it reaches values of roughly 20° at 14.5 km. The minimum and intermediate compressive stress axes roughly mirror one another about the 45° plunge angle for each of the three cases. At the fault, the minimum and intermediate axes go from ∼30° and ∼60°, respectively, near the surface, to ∼45° for both at midcrustal depths, to ∼30° and ∼45°, respectively, in the lower crust. The fact that these axes are not oriented parallel and perpendicular to the free surface at the 0.5 km depth will be discussed in section 4.2.

The half-space approximation model shows no variation in the plunge angle of the three axes away from the fault, with the intermediate axis at 90° and the other two at 0°. This orientation is what would be expected in a classic Andersonian tectonic regime. In the two finite width shear zone models, however, the intermediate and minimum compressive stress axes exhibit local maxima or minima above the shear zone lateral boundary. This feature is most noticeable in the 14.5 km depth figures, where these two axes go from their Andersonian orientation in the far field, to plunge angles of roughly 30° and 60° above the shear zone boundary, and back to an Andersonian orientation above the shear zone. This is the result of the concentration of shear and normal stresses at the shear zone corners seen in Plates 2 and 4.

3.7. Visualization of the Stress Tensor in the Seismogenic Zone

As we have seen in section 3.6, the deviatoric stress tensor is not oriented in a classical Andersonian way in the lower crust. The presence and relative magnitude of the horizontal shear stress, as well as the concentration of shear and normal stress near the shear zone corners, cause the principal axes to rotate about horizontal axes, making an examination of the maximum compressive stress plotted in the horizontal plane alone (as in section 3.4) an inadequate way of describing the stress state. As a partial solution to this problem, we present here the stress tensor plotted as so-called "beach ball" diagrams, using a method for plotting moment tensors.

In order to plot the stress tensor as a beach ball, we decompose the full stress tensor ($\boldsymbol{\sigma}$) and plot only what is equivalent to the major double couple component of the moment tensor, represented by the tensor [after *Jost and Herrmann,* 1989]

$$\sigma_3^*(\mathbf{v}_3\mathbf{v}_3 - \mathbf{v}_2\mathbf{v}_2), \tag{1}$$

where σ_3 is the most negative eigenvalue (most compressive principal stress) of $\boldsymbol{\sigma}$; σ_i^* is the deviatoric

part of the eigenvalue, given by

$$\sigma_i^* = \sigma_i - \frac{1}{3}(\sigma_1 + \sigma_2 + \sigma_3); \quad (2)$$

$\mathbf{v}_i = (v_{ix}, v_{iy}, v_{iz})$ is the eigenvector of σ associated with σ_i which forms the dyadic tensor by

$$\mathbf{v}_i\mathbf{v}_i = \begin{bmatrix} v_{ix}^2 & v_{ix}v_{iy} & v_{ix}v_{iz} \\ v_{ix}v_{iy} & v_{iy}^2 & v_{iy}v_{iz} \\ v_{ix}v_{iz} & v_{iy}v_{iz} & v_{iz}^2 \end{bmatrix}. \quad (3)$$

The dyadic tensor describes a dipole in the direction of the given eigenvector.

This representation of the stress tensor allows us to visualize the orientations of all three of the principal stresses. Figure 7 shows an illustration of the stress tensor beach ball. The most and least compressive principal stress axes are oriented at 45° to the nodal planes, and the intermediate principal axis lies along the intersection of the nodal planes. The orientation of the maximum compressive stress with respect to the fault plane (θ) is also printed above the beach ball.

The danger with this representation is the association of beach balls with focal mechanisms for earthquakes. Nodal planes for focal mechanisms are the two possible slipping planes, whereas for the stress tensor they are the planes of maximum shear stress. The P and T axes of focal mechanisms can therefore be quite different from the maximum and minimum compressive stress axes. If brittle fracture in the crust occurs on planes between 30° and 60° (and perhaps $> 60°$) from the maximum compressive stress direction, we would expect there to be as much as 15° difference between the nodal planes presented here and potential fault planes.

Figures 8-10 show the stress tensor beach balls for the three cases before and after the earthquake. The plots are of a cross section covering the elastic thickness of the upper crust (0-15 km) and the uppermost, 3-km-thick layer of the viscoelastic shear zone and from the fault out to a lateral distance of 90 km, beyond which the results change little. A beach ball is plotted at each node, with some nodes near the fault omitted where they are closer together and results are redundant. Even with these omissions, there is a greater density of beach balls near the fault due to the concentration of elements there. Though Figures 8-10 are cross sections, the stress tensors are plotted in their conventional map view orientation (i.e., they were rotated 90° about the x axis) to facilitate viewing multiple depths simultaneously.

Much like in sections 3.1-3.6, the three plots are qualitatively the same at the fault. The upper two thirds of the fault show orientations of the maximum compressive stress at $66° - 77°$ with respect to the fault before the earthquake and ~90° after the earthquake. The lower portion of the fault has orientations of $46° - 58°$ both before and after the earthquake. From the beach balls we can also see the plunge of the maximum compressive stress, as well as the orientation of the other two principal stress axes. In both time snap shots, there is a rotation of the beach balls from the top to the bottom of the fault that can be seen most clearly in the orientation of the intermediate principal stress. The axis is nearly vertical at the top of the fault and rotates toward the horizontal plane and pointing nearly along strike at the bottom of the fault. This rotation is especially clear in the postearthquake plots, where one of the planes of maximum shear is nearly coplanar with the horizontal plane near the bottom of the fault.

Away from the fault, stress orientations are simpler, with the intermediate principal stress near vertical for most of the crust. The exception to this is in the elastic crust above the shear zone boundary for cases 2 and 3. Near 35 km from the fault in Figure 9, the lateral extent of the viscoelastic shear zone, the intermediate stress axis again rotates toward the horizontal plane but in the opposite sense in comparison to the rotation at the base of the fault. The result is similar, though, in that one of the planes of maximum shear is rotated toward a horizontal orientation. It is interesting to note that the fact that the rotation is in the opposite sense in comparison to that at the fault is not possible to discern from the plunge angles shown in section 3.6, since there is no measurement of whether the principal axes lie above or below the horizontal plane. The state of stress in the remaining crust is described reasonably well with the orientation of the maximum principal compressive stress, as it lies within the horizontal plane.

4. Discussion

4.1. Stress Results

In our numerical models of crustal stress the three controlling factors for the concentration of shear stress in the vertical plane (σ_{xy}) at any given point are its depth, its proximity to the shear zone, and its proximity to the fault. The constant velocity boundary conditions lead to a state of simple shear, so that the vertically averaged shear stress is the same for

all depth profiles. Since the viscoelastic shear zone cannot sustain any shear stress over the duration of the earthquake cycle, the elastic crust above the shear zone must accommodate the same total shear stress over its depth of 15 km as the elastic crust away from the shear zone accommodates over its depth of 50 km. As a result of this, models with a finite width shear zone see a dramatic increase in shear stress in the upper crust near the fault when compared to the far field, as seen in Plate 2. The slight increase in shear stress midway between the fault and the boundary seen in the preearthquake time step of case 1 is most likely due to the use of a low-viscosity Maxwell solid for the lower crust and its tendency to broaden the zone of high deformation within the crust, as pointed out by *Roy* [1998].

While the effect of the finite width shear zone on the upper crust is clear, the actual width chosen does not significantly affect the state of stress on the fault. During the initial buildup of shear stress to the first earthquake the fault is loaded equally at all depths. Once a regular earthquake cycle is established, however, stress becomes concentrated at the base of the fault as a result of the loading and unloading of the shear zone beneath the fault. The shear stress at the base of the fault does not drop completely to zero during the earthquake in our solution because of the high stress gradient at the fault tip. The extreme gradient is approximated linearly and becomes "smeared" over two to three finite elements, thereby artificially increasing the amount of shear stress on the lower fault element faces immediately after an earthquake (see Appendix A). Above these elements, however, the shear stress on the fault is significantly lower than in the crust more than 15-20 km (or one fault depth) away from the fault at all times. This "stress trough" due to the fault has been observed in other models as well [*Lyzenga et al.,* 1991; *Verdonck and Furlong,* 1992].

The shear stress in the horizontal plane (σ_{yz}) is close to zero everywhere but within a radius of 5 km from the fault tip, where it is of the same order of magnitude as the shear stress in the vertical plane. Each earthquake causes a shearing between the elastic upper crust and viscoelastic lower crust near the fault tip, which creates the "basal" shear stress in this zone. This component of the total shear stress affects such a narrow zone near the fault that the results are indifferent to the width of the shear zone. In the beach ball diagrams (Figures 8-10) it can be seen that the basal shear stress causes one of the maximum shear stress planes to rotate toward a horizontal orientation in this region, while the component of shear stress parallel to the fault rotates the other plane of maximum shear stress toward a vertical orientation (coplanar with the fault plane). This is the result of the two components of shear stress being roughly equal in magnitude at the base of the fault, and moreover, it indicates that they are both significantly greater in magnitude than the 20-MPa normal stress. This region of the mesh is where our solution is least accurate with regards to stress levels (see Appendix A). However, the inaccuracy of the solution here is only of major concern for the immediately postearthquake snapshots, since the solution has had enough time to re-equilibrate by the preearthquake snapshot.

The relative importance of the normal component of the stress tensor as it relates to the San Andreas Fault in California warrants some discussion here. Though very little strain normal to the fault has been observed geodetically [e.g., *Argus and Gordon,* 1991; *Kelson et al.,* 1992; *Savage and Simpson,* 1998], there is ample geologic and seismic evidence for the San Andreas Fault system being a transpressive plate boundary [*Namson and Davis,* 1988; *Bloch et al.,* 1993; *Jones et al.,* 1994]. The stress data in California do not appear unreasonable, then, with respect to such observations, so long as a suitable explanation can be found for the San Andreas Fault's dominantly strike-slip behavior.

Our calculation of normal stress (Plate 4) shows a concentration of stress above the finite width shear zones in cases 2 and 3 due to the effective thinning of the elastic crust, similar to the concentration of shear stress in the same region discussed above. The result of this is that the maximum compressive stress shows little change in its orientation from the far field, where stress levels are overall lower, to the higher stress areas over the viscoelastic shear zone. The reason for this is that while the elevated shear stress above the shear zone tends to rotate the maximum compressive stress toward lower angles, the elevated normal stress tends to rotate the MCS in the opposite direction. Therefore the finite width shear zone models have similar MCS results as the half-space approximation model.

However, our calculation of normal stress ignores any possible contribution from the shear zone, simply assuming that the timescale over which the normal stress develops is much greater than the Maxwell relaxation time of the viscoelastic solid. There are, of course, other possibilities. For example, as a first-

order approximation of fault-normal stress, we first tried a constant amount of stress to be added to the σ_{xx} component of the stress tensor at all nodes in the mesh. The assumption of a constant normal stress is reasonable in the half-space approximation model, since the lower viscoelastic portion of the model cannot maintain any stress. In this case, it is equivalent to the assumption that the crustal block is under a constant load, normal to the fault, similar to the calculation discussed in section 3.3. In the finite width shear zone models, however, this is most likely a poor approximation. Although the shear zone is defined to be viscoelastic in its shear modulus only, and not in bulk modulus, it will relieve normal stresses through shearing nonetheless by essentially "squeezing" out the ends and bottom of the mesh. Were this not the case, and the viscoelastic material were not allowed to escape the shear zone channel, then the shear zone would behave elastically in compression. The result of this would be our first-order approximation of the fault-normal stress, i.e., constant at all points throughout the domain. As an example of the consequences of this simplified assumption for the normal stress, we show in Figure 11 the orientation of the MCS as a function of distance from the fault for the wide shear zone model, where it can be seen that the MCS rotates to much higher angles ($75° - 80°$) away from the shear zone than in the previously presented results (i.e., Figure 3).

Interestingly, this result has some similarity to the data described by *Hardebeck and Hauksson* [1999], where in profiles across the SAF in southern California, they found that the MCS rotates from high angles ($80° - 90°$) far from the SAF to angles closer to the expected brittle fracture orientation ($30°-60°$) in close proximity to the SAF. The interpretation of these data is the source of some controversy [*Scholz,* 2000]. If rock fracture experiments are a reasonable analog for fault behavior, then the maximum compressive stress (MCS) should make an angle of $\sim 30°$ with respect to the fault plane (based on a static coefficient of friction of 0.6 [*Byerlee,* 1978]). Elevated pore pressures or inherently weak materials within the fault zone can rotate the MCS to angles to 45° [*Byerlee,* 1990; *Rice,* 1992], and preexisting planes of weakness can further rotate the MCS to 60° [*Sibson and Xie,* 1998]. However, an MCS at nearly 90° to slipping strike-slip fault planes [*Zoback and Beroza,* 1993; *Hauksson,* 1994] and zones of rotated maximum compressive stresses much wider than the fault zone (of the order of tens of kilometers [*Hardebeck and Hauksson,* 1999]) are difficult to explain with these models. Though the boundary conditions for the results shown in Figure 11 are somewhat awkward to justify, the possibility that finite width shear zones may provide an alternative explanation for wide zones of near fault MCS rotation is intriguing and merits further investigation. Additionally, stresses in California are inferred from boreholes or seismic data, which generally have resolving power in either the upper or mid to lower crust, respectively. If stress orientations are a function of depth, as seen with our model, then this might explain discrepancies between the two data sets (e.g., *Hardebeck and Hauksson* [1999] versus *Mount and Suppe* [1992]).

4.2. Plunge Angles of Principal Axes: Possible Key?

The rotation of the principal stress axes seen in Figures 6 and 8-10 implies that a finite width shear zone may leave some signature in the stress orientations in the upper crust. Specifically, the concentration of stress above the shear zone and at its corners cause the stress tensor to rotate away from its Andersonian orientation. This rotation is minimal in the maximum compressive stress axis but approaches 45° for the minimum and intermediate principal axes. In both of the finite width shear zone models this rotation can be seen most clearly at depths near the elastic-viscoelastic boundary. Because of the small Maxwell relaxation time of the shear zone in relation to the earthquake repeat time, this boundary approximates a traction-free boundary condition. Therefore shear stresses in the horizontal plane must approach zero, and the principal stress axes should align with the horizontal plane in an Andersonian fashion. This is seen in the finite width shear zone models at distances of 10 to 30 km away from the fault for the wide shear zone model and 5 km from the fault for the narrow shear zone model, corresponding to the widths of the shear zones in each model. Beyond those distances, however, we see the rotation of the principal axes such that the plunge angles of the intermediate and minimum compressive axes are $35° - 40°$ and $50° - 55°$, respectively.

The Earth's surface is also a traction free boundary and should therefore align the principal stress axes with the horizontal plane. In Figure 6 it can be seen that at the 0.5 km depth this is not the case. However, in Figure 12 we show the total horizontal shear stress ($\sqrt{\sigma_{xz}^2 + \sigma_{yz}^2}$) as a function of depth

at the fault before and after an earthquake. Using this measure, we can see that the upper surface of our mesh is approaching that of a traction-free surface. In other words, though the plunge angles indicate that the minimum and intermediate principal stress axes are not aligned with the free surface, in fact, the magnitudes of these principal stresses are approaching zero, and therefore their orientations are somewhat meaningless. Figure 12 also shows that before the earthquake, the viscoelastic shear zone (below 15 km depth) is completely relaxed, and after the earthquake, shear stress is concentrated at the elastic-viscoelastic boundary, where it reaches its maximum value.

In their study of northern California faults, *Bokelmann and Beroza* [2000] found a similar maximum in their proxy for the horizontal shear stress derived from moment tensor solutions, though at depths of 5 to 9 km. In our models this depth is controlled by the transition from the elastic to viscoelastic material models. Were we to smooth this transition further, such that it took place more gradually from 10 to 20 km (instead of 15 to 18 km), we would see the horizontal shear stress reach a higher values at shallower depths. Beneath this maximum, *Bokelmann and Beroza* [2000] see a gradual decrease in the horizontal shear stress and interpret this as the transition from a brittle upper crust to a weaker lower crust. While this general result agrees well with our modeling results, it does not favor any one of the case geometries examined over another. However, it does indicate that if work of this kind could be extended to examine changes horizontal shear stress as a function of lateral distance from the fault, it may be possible to detect some signature of a finite width shear zone.

4.3. Modeling Considerations and Limitations

It should be pointed out that the models used here are as simple as possible while still effectively testing hypotheses about the lower crust. Certainly, the material models, shear zone geometries, and fault failure mechanisms presented here do not represent the real earth, yet the models exhibit certain features relevant to the earthquake cycle and observations of stress in California. Some issues related to our modeling simplifications are as follows:

1. The material models used here are all linear, and the velocity boundary conditions imposed at the domain edges are constant in time. However, the loading of the fault is nonlinear in time once the cycling of earthquakes is introduced. To clarify this point, in Figure 13 we show the stress tensor beach balls for the half-space approximation model before and after the first earthquake to occur in model time. This plot is substantially different from Figure 8, which is the same model at a later time in the calculation. Before the first earthquake the crust is in simple shear, and normal and shear stresses at all depths are constant, as seen by the identical beach balls and maximum compressive stress orientations in Figure 13a. In the postearthquake snapshot, while Figures 8b and 13b are similar, the concentration of stress at the base of the fault is more noticeable for the mature fault zone. As more earthquake cycles occur, the concentration of shear stress increases in the viscoelastic shear zone, causing it to load the overlying fault rapidly and nonlinearly immediately following an earthquake. The most noticeable effect of using a non-Newtonian power law flow rheology would likely be an even greater localization of stresses at the base of the fault, as was seen with similar modeling done by *Lyzenga et al.* [1991].

Figure 1

2. A finite width shear zone concentrates stresses above the shear zone. The geometry for the shear zone used here was a simple "channel" of viscoelastic elements, uniform in thickness and width. However, the concentration of stress above the channel is a general result, and altering the geometry of the shear zone would mainly affect the magnitude of the stresses in the upper crust. For example, a shear zone that is narrow at the top and wider with depth would lead to a more gradual increase in the stress magnitudes from the model edge to the fault, rather than the abrupt change seen at the shear zone boundary here.

3. The fault failure criterion used here is based on a threshold average shear stress on the fault, and once the threshold is exceeded, the entire fault slips without friction. These simplifications lead to earthquakes with complete stress drops and large stress concentrations at the base of the fault. Our model is therefore in the weak fault category for the San Andreas, in which stress drops associated with large events ($\sim$10 MPa) are assumed to relieve all shear stress on the fault. This model is supported by the previously discussed stress observations in California as well as arguments from heat flow data [*Lachenbruch and Sass*, 1980], and we feel it is therefore reasonable. However, our model failure mechanism does not allow for postseismic slip, creep, or nonprincipal (i.e., smaller) events. These mechanisms for strain re-

lease may be justifiably neglected in the present study though, since the overwhelming majority of seismic moment release on the San Andreas has been from principal, strike-slip events [e.g., *Bakun,* 1999].

5. Conclusions

Using finite element models of an elastic crust overlying a viscoelastic shear zone, we have shown the effects of varying the width of the shear zone on stress orientations in the elastic portion of the crust. Three model cases were considered: a half-space approximation model, with a shear zone that is essentially infinite in its width; a wide shear zone model of 70 km width; and a narrow shear zone model of 10 km width. While the effects of the width of the shear zone on the orientation of the maximum compressive stresses were remarkably small, there were significant differences among the three models when the plunge angles of the principal stress axes were examined. Most notably, the intermediate and minimum compressive stress axes dipped away from their Andersonian orientations at the Earth's surface (of either 90° or 0°) to plunge angles approaching 45° near the elastic-viscoelastic boundary depth and near the finite width shear zone boundaries. This change in plunge angle is the result of stress concentrations above the finite width viscoelastic shear zone, and it implies that stress orientations near faults can change as a function of lateral distance from the fault, and perhaps more importantly, there can be large variations with depth.

The effect of a finite width shear zone with a Maxwell relaxation time that is much less than the earthquake repeat time is to attenuate the elastic thickness of the crust near the fault. Since the depth averaged shear and normal stresses must be equal over any depth profile along the width of the mesh, the thinner elastic crust over the shear zone must then accommodate a greater concentration of stress over its depth than does the thicker elastic crust away from the shear zone. The distribution of this stress in the upper elastic crust is also governed by the slow concentration of stress at the elastic-viscoelastic boundary over many earthquake cycles and would not be observed in models that only consider a single event. Additionally, the concentration of shear stress at the base of the fault in both the horizontal and vertical planes leads to large variations in the orientation of the stress tensor with depth at the fault.

While our original hypothesis in this study was that finite width shear zones may help to explain maximum compressive stresses that are almost perpendicular to major strike-slip faults in California, we found that unless the shear zone is somehow constrained so that it acts elastically in compression but viscoelastically in shear, this hypothesis was incorrect. However, the rotations of the principal stress axes near the shear zone borders that we observed in the upper crust may prove useful in determining the nature of the deformation in the lower crust, especially given recent advances in the acquisition and interpretation of stress data from earthquake focal mechanisms and moment tensors.

Appendix A: Element Resolution at the Fault Tip

Solving for stresses near the tip of the fault plane poses a difficult problem in the finite element method. While it is not strictly a singularity, the concentration of stress at the transition from a freely slipping surface to a continuum is very large. As this region of the mesh is of great interest, we ran some simple tests to determine the capability of our method to resolve those stresses.

In our model, earthquakes are simulated by allowing the two fault surfaces to slide freely for one time step. The symmetric boundary conditions mean that each node on one side of the fault will move an equal and opposite distance with respect to its starting point as each corresponding node on the opposite side of the fault. It also means that nodes directly below the fault (in the lower half of the $x = 0$ plane) will remain in their original positions for the entire model run. While this lower continuation of the fault plane does not experience any deformation, it does defuse stress viscoelastically. However, in the time step immediately following an earthquake the viscoelastic material is responding elastically, since the earthquake takes place on a timescale much smaller than the Maxwell relaxation time. It is this time step, and the transition on this plane from the moving upper fault surface to the immobile lower "fault zone," that we focus on here.

Our model resolution experiment was designed to explore these issues without any additional complications. As an introduction to our approach, consider the following thought experiment: If a shearing motion is enforced on one face of a cube while the opposite face is held motionless (zero displacement), the cube will exhibit a constant shear stress throughout

its domain. This situation is analogous to the models presented in this paper during the interseismic period, where the moving face of the cube is like one of the moving edges of our model domain, and the zero displacement face is like the fault plane within the model domain. In order for our thought experiment to be analogous to our models during an earthquake, instead of holding the entire "fault plane" face of the cube fixed, we fix only one half of the face and define the other half of the face as a free or zero traction surface. In this way, the fixed half of the face is like the lower continuation of the fault in our model, and the upper half is like the freely slipping fault plane. Our resolution experiment, then, is to determine the effect of element size on the solution near the fault plane.

Plate 5 shows an example of the mesh that we used for these tests. The basic, low-resolution mesh, case 1, is a cube of elements, 8x8x8 (elements are 1x1x1). Cases 2 and 3 are meshes of 16x8x16 elements (shown, with elements that are $\frac{1}{2}$x1x$\frac{1}{2}$) and 32x8x32 elements (elements are $\frac{1}{4}$x1x$\frac{1}{4}$), respectively. Because of our 2-D approximation for the models presented in this paper, we were not concerned with the resolution in the along strike direction, and we therefore only altered the number of elements in the downdip direction and fault perpendicular direction. Also shown in Plate 5 are contours of shear stress, with the boundary between the held and free portions of the cube's fault plane face clearly seen.

To compare the different resolutions, we examine the two components of shear stress relevant to our models for a profile across the cube. The profile shows the stresses at nodes along a line from the bottom of the fault face to the top, centered along the fault, as shown by the red line in Plate 5. In Figure A1 the component of shear stress that is parallel to the cube face (σ_{xy}, thin lines) and the component of shear stress in the horizontal plane (σ_{yz}, thick lines) are shown for the three resolution tests: 8x8x8, 16x8x16, and 32x8x32.

There are two important features in Figure A1. First, we expect σ_{xy} to be zero on the fault (abcissa distance > 4). This is numerically realized about two to three elements away from the fault tip. Second, for the constrained portion of the graph (≤ 4) the two lower-resolution models agree well with the higher-resolution model at one element away from the fault tip (i.e., at $z = 3$ for case 1, and at $z = 3.5$ for case 2). The mesh used for our fault model most closely resembles the 16x8x16 mesh in terms of resolving power. For these reasons, we feel confident that the mesh presented in this paper can sufficiently resolve the stresses within two elements of the fault tip.

Acknowledgments. The authors would like to acknowledge the support of Centric Engineering Inc. (now Ansys Corp.) in the use of their finite element software, Spectrum, and are especially indebted to Robert Ferencz at Lawrence Livermore National Laboratory (formerly of Centric Engineering). This work was supported by a Cooperative University/Laboratory Reseach (CULAR) grant to M.A.R. and was performed in part under the auspices of the U. S. Department of Energy by Univeristy of California Lawrence Livermore National Laboratory under contract No. 01-GS-007. The majority of the calculations were done on an SGI Challenge machine at UC Davis, and the authors would like to thank Louise Kellogg and Paul Waterstraat at UC Davis for facilitating the work done there, and Doug Neuhauser and Charley Paffenbarger of the UC Berkeley Seismological Laboratory for facilitating the computing done at Berkeley. We would also like to thank Roland Bürgmann for his input and help, and James Savage, Mousumi Roy and Fred Pollitz for their careful reviews of this manuscript.

References

Anderson, E. M., *The Dynamics of Faulting and Dyke Formation,* 2nd ed., 206 pp., Oliver and Boyd, White Plains, N.Y., 1951.

Argus, D. F., and R. G. Gordon, Current Sierra Nevada-North American motion from very long baseline interferometry: Implications for the kinematics of the western United States, *Geology, 19,* 1085-1088, 1991.

Bakun, W. H., Seismic activity of the San Francisco Bay region, *Bull. Seismol. Soc. Am., 89,* 764-784, 1999.

Bloch, R. B., R. Von Huene, P. E. Hart, and C. M. Wentworth, Style and magnitude of tectonic shortening normal to the San Andreas fault across Pyramid Hills and Kettleman Hills South Dome, California, *Geol. Soc. Am. Bull., 105,* 464-478, 1993.

Bokelmann, G. H. R., and G. C. Beroza, Depth-dependent earthquake focal mechanism orientation: Evidence for a weak zone in the lower crust, *J. Geophys. Res., 105,* 21,683-21,695, 2000.

Byerlee, J. D., Friction of rocks, *Pure Appl. Geophys., 116,* 615-626, 1978.

Byerlee, J. D., Friction, overpressure and fault normal compression, *Geophys. Res. Lett., 17,* 2109-2112, 1990.

Cohen, S. C., A multilayer model of time-dependent deformation following an earthquake on a strike-slip fault, *J. Geophys. Res., 87,* 5409-5421, 1982.

Ellsworth, W. L., Earthquake history, 1769-1989, in *The San Andreas Fault System, California,* edited by R. E. Wallace, Chap. 6, *U.S. Geol. Surv. Prof. Pap., 1515,*

153-188, 1990.

Hardebeck, J. L., and E. Hauksson, Role of fluids in faulting inferred from stress field signatures, *Science, 285,* 236-239, 1999.

Hauksson, E., State of stress from focal mechanisms before and after the 1992 Landers earthquake sequence, *Bull. Seismol. Soc. Am., 84,* 917-934, 1994.

Hughes, T. J. R., *The Finite Element Method,* 803 pp., Prentice-Hall, Old Tappan, N. J., 1987.

Jones, D. L., R. Graymer, C. Wang, T. V. McEvilly, and A. Lomax, Neogene transpressive evolution of the California Coast Ranges, *Tectonics, 13,* 561-574, 1994.

Jost, M. L., and R. B. Herrmann, A student's guide to and review of moment tensors, *Seismol. Res Lett., 60,* 37-57, 1989.

Ju, J.-W., and R. L. Taylor, A perturbed lagrangian formulation for the finite element solution of nonlinear frictional contact problems, *J. Theor. Appl. Mech., 7,* suppl. 1-14, 1988.

Kelson, K. I., W. R. Lettis, and M. Lisowski, Distribution of geologic slip and creep along faults in the San Francisco Bay region, in *Proceedings of the Second Conference on Earthquake Hazards in the Eastern San Francisco Bay Area,* edited by G. Borchardt et al., *Spec. Publ. Calif. Div. Mines Geol., 113,* 31-38, 1992.

Lachenbruch, A. H., and J. H. Sass, Heat flow and the energetics of the San Andreas Fault zone, *J. Geophys. Res., 85,* 6185-6222, 1980.

Lisowski, M., J. C. Savage, and W. H. Prescott, The velocity field along the San Andreas Fault in central and southern California, *J. Geophys. Res., 96,* 8369-8389, 1991.

Lyzenga, G. A., A. Raefsky, and S. G. Mulligan, Models of recurrent strike-slip earthquake cycles and the state of crustal stress, *J. Geophys. Res., 96,* 21,623-21,640, 1991.

Mount, V. S., and J. Suppe, Present-day stress orientations adjacent to active strike-slip faults: California and Sumatra, *J. Geophys. Res., 97,* 11,995-12,013, 1992.

Namson, J. S., and T. L. Davis, Seismically active fold and thrust belt in the San Joaquin Valley, Central California, *Geol. Soc. Am. Bull., 100,* 257-273, 1988.

Nur, A., and G. Mavko, Postseismic viscoelastic rebound, *Science, 183,* 204-206, 1974.

Pollitz, F. F., and I. S. Sacks, Modeling of postseismic relaxation following the great 1857 earthquake, Southern California, *Bull. Seismol. Soc. Am., 82,* 454-480, 1992.

Prescott, W. H., and A. Nur, The accomodation of relative motion at depth on the San Andreas fault system in California, *J. Geophys. Res., 86,* 999-1004, 1981.

Rice, J. R., Fault stress states, pore pressure distributions, and the weakness of the San Andreas Fault, in *Fault Mechanics and Transport Properties of Rock,* edited by B. Evans and T. F. Wong, pp. 475-503, Academic, San Diego, Calif., 1992.

Roy, M., Evolution of fault systems at a strike-slip plate boundary: A viscoelastic model, *Geophys. Res. Lett., 25,* 2881-2884, 1998.

Savage, J. C., Equivalent strike-slip earthquake cycles in half-space and lithosphere-asthenosphere Earth models, *J. Geophys. Res., 95,* 4873-4879, 1990.

Savage, J. C., and R. O. Burford, Accumulation of tectonic strain in California, *Bull. Seismol. Soc. Am., 60,* 1877-1896, 1970.

Savage, J. C., and W. H. Prescott, Asthenosphere readjustment and the earthquake cycle, *J. Geophys. Res., 83,* 3369-3376, 1978.

Savage, J. C., and R. W. Simpson, Strain accumulation rates in the San Francisco Bay area, 1972-1989, *J. Geophys. Res., 103,* 18,309-18,051, 1998.

Scholz, C. H., Evidence for a strong San Andreas Fault, *Geology 28,* 163-166, 2000.

Sibson, R. H., and G. Xie, Dip range for the intracontinental reverse fault ruptures: Truth not stranger than friction?, *Bull. Seismol. Soc. Am., 88,* 1014-1022, 1998.

Thatcher, W., Nonlinear strain buildup and the earthquake cycle on the San Andreas fault, *J. Geophys. Res., 88,* 5893-5902, 1983.

Verdonck, D., and K. P. Furlong, Stress accumulation and release at complex transform plate boundaries, *Geophys. Res. Lett., 19,* 1967-1970, 1992.

Zatman, S., On steady rate coupling between an elastic upper crust and a viscous interior, *Geophys. Res. Lett., 27,* 2421-2424, 2000.

Zhong, Z.-H., and J. Mackerle, Static contact problems–A review, *Eng. Comput., 9,* 3-37, 1992.

Zienkiewicz, O. C., and R. L. Taylor, *The Finite Element Method,* vol. 2, 807 pp., McGraw-Hill, New York, 1991.

Zoback, M. D., and G. C. Beroza, Evidence for near-frictionless faulting in the 1989 (M 6.9) Loma Prieta, California, earthquake and its aftershocks, Geology, *21,* 181-185, 1993.

Zoback, M. D., et al., New evidence on the state of stress of the San Andreas Fault system, *Science, 238,* 1105-1111, 1987.

Zoback, M. L., and M. D. Zoback, Faulting patterns in north-central Nevada and strength of the crust, *J. Geophys. Res., 85,* 275-284, 1980.

J. C. Lynch and M. A. Richards, Department of Earth and Planetary Science, University of California, Berkeley, CA 94720,USA. (lynch@seismo.berkeley.edu; markr@seismo.berkeley.edu)

Received September 28, 2000; revised May 4, 2001; accepted May 5, 2001.

This preprint was prepared with AGU's LaTeX macros v5.01. File JGR˙2001 formatted November 30, 2001.

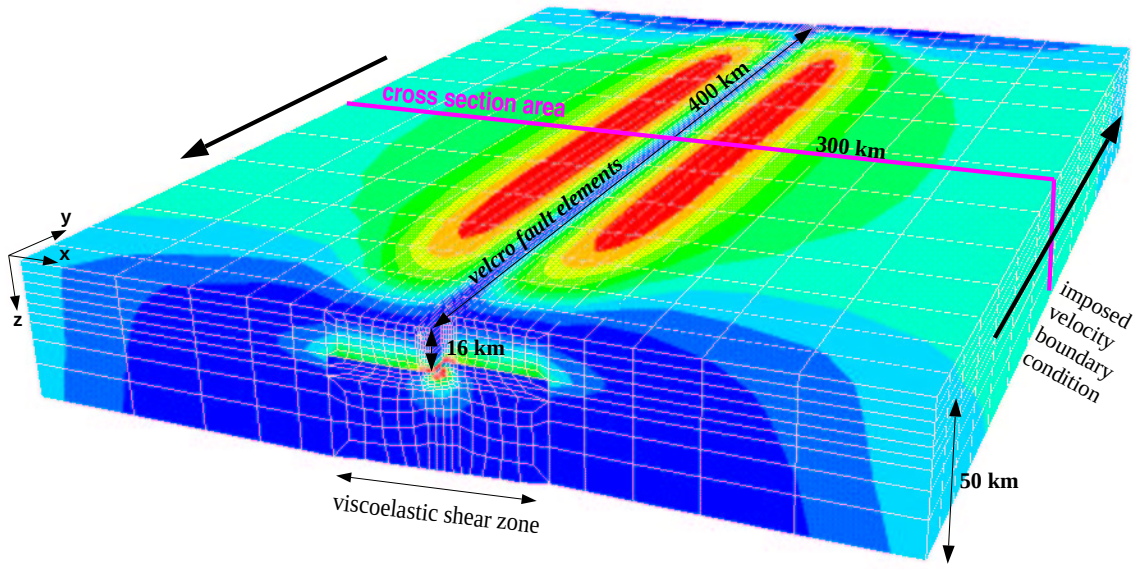

Plate 1. The finite element mesh for case 2, the wide shear zone model. Shown are contours of shear stress in the vertical plane (σ_{xy}) immediately following an earthquake, as evidenced by the concentration of stress in the shear zone beneath the fault and the relative lack of stress on the fault itself. Also shown is the accumulated displacement at the steady state solution, multiplied by a factor of 100. The pink lines indicate the cross section plane at which the solution is used for the all of the rest of the figures (hence, our modeling is 2.5-D). The viscoelastic shear zone in this case is 70 km wide and is centered beneath the fault. The velcro fault elements run the entire length of the mesh. Constant velocity boundary conditions are imposed at the mesh edges, parallel to the fault.

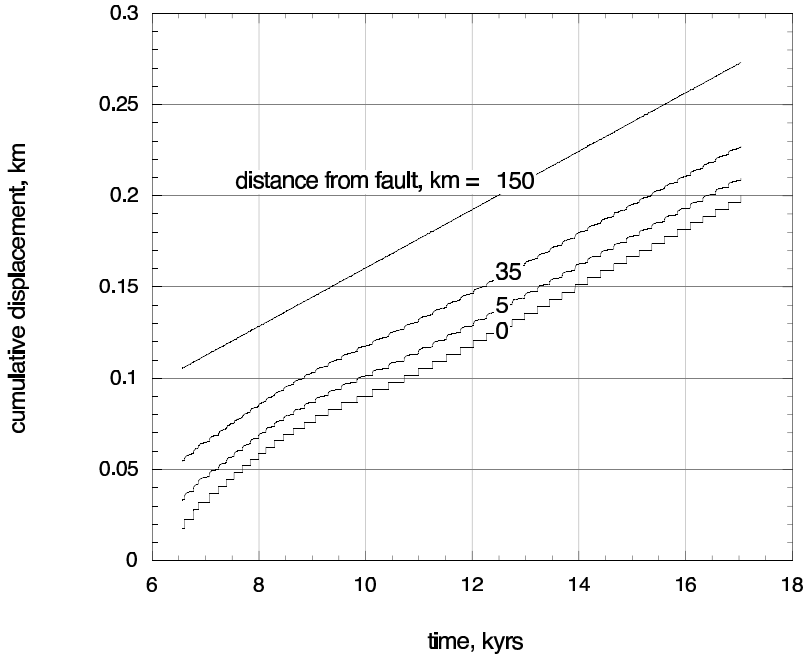

Figure 1. Displacement versus time for four surface nodes showing the development toward the limit cycle. The nodes are 150, 35, 5, and 0 km from the fault. The time before the first earthquake is not shown. The node at the fault shows stick-slip behavior, while the node at the boundary reflects the constant velocity boundary condition. A long-period transient can be seen that affects the amount of slip and amount of time between earthquakes for roughly the first 6000 years, after which the model settles into a regular cycle.

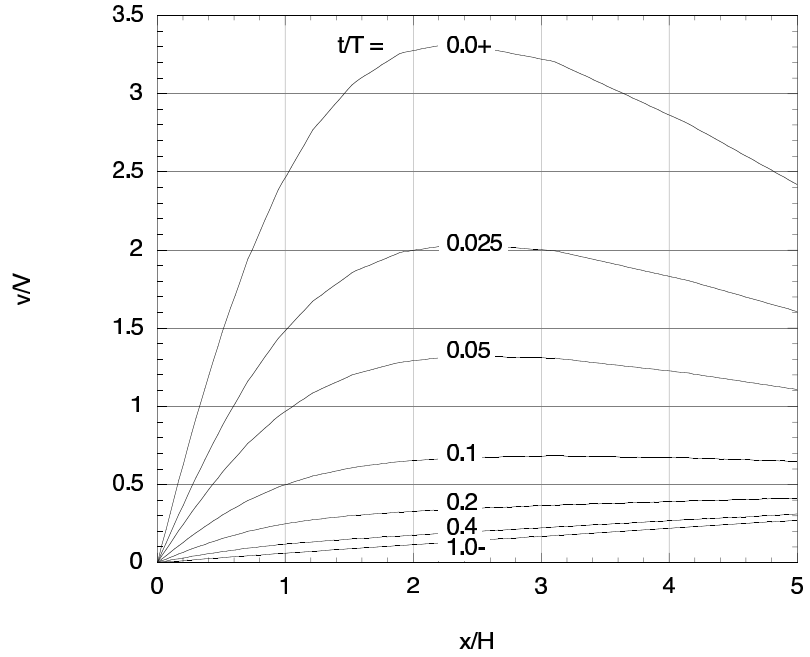

Figure 2. Velocity profiles at the surface for various times in a mature earthquake cycle. Distance from the fault is shown normalized by the depth of the fault, H; velocity is normalized by the far-field velocity, V; and time is normalized by the earthquake repeat time, T.

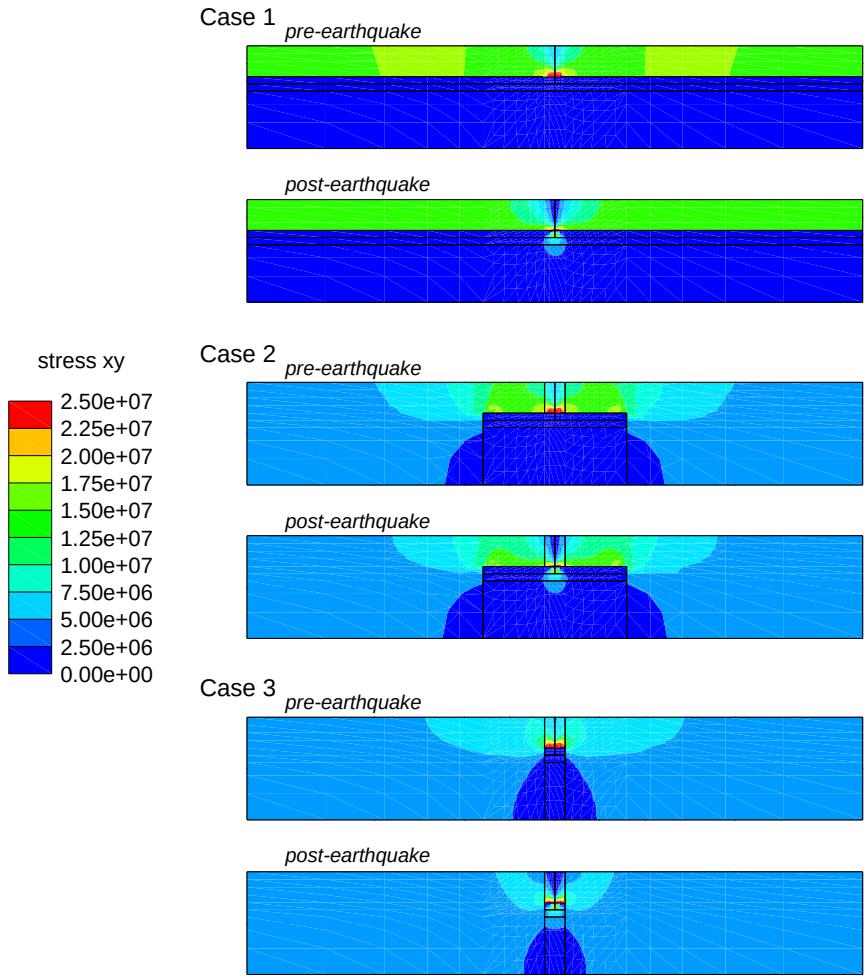

Plate 2. Cross sections of vertical shear stress contours (σ_{xy}) for the three model cases: Case 1 is the half-space approximation, case 2 is the wide shear zone (70 km), and case 3 is the narrow shear zone. Preearthquake and postearthquake time steps are shown. The scale is in pascals. Concentration of shear stress above the shear zone is evident in the two finite width shear zone models. Note that the vertical lines parallel to the fault line are a result of the mesh discretization and visualization but do not signify a change in material parameters within the elastic upper crust.

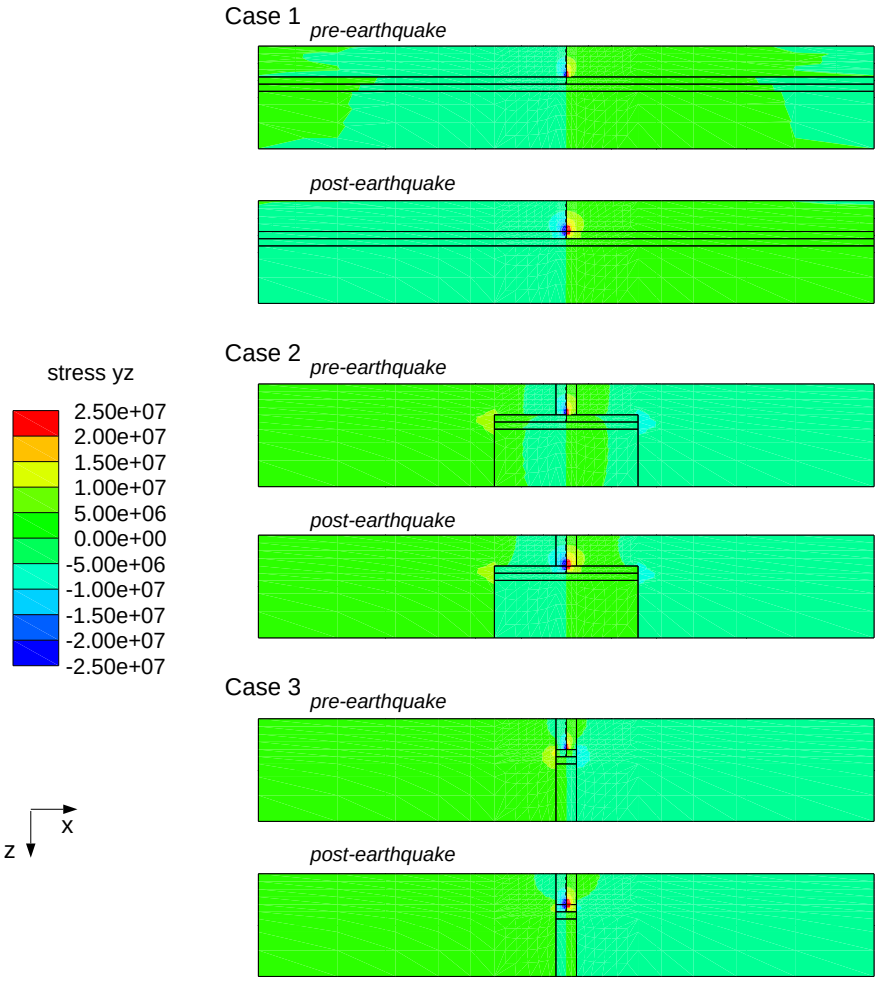

Plate 3. Cross sections of shear stress in the horizontal plane (σ_{yz}) contours for the three model cases and the preearthquake and postearthquake time steps. The scale is in pascals. Concentration of horizontal shear is at the fault tip, on the boundary between the elastic and viscoelastic material models, and is near zero elsewhere.

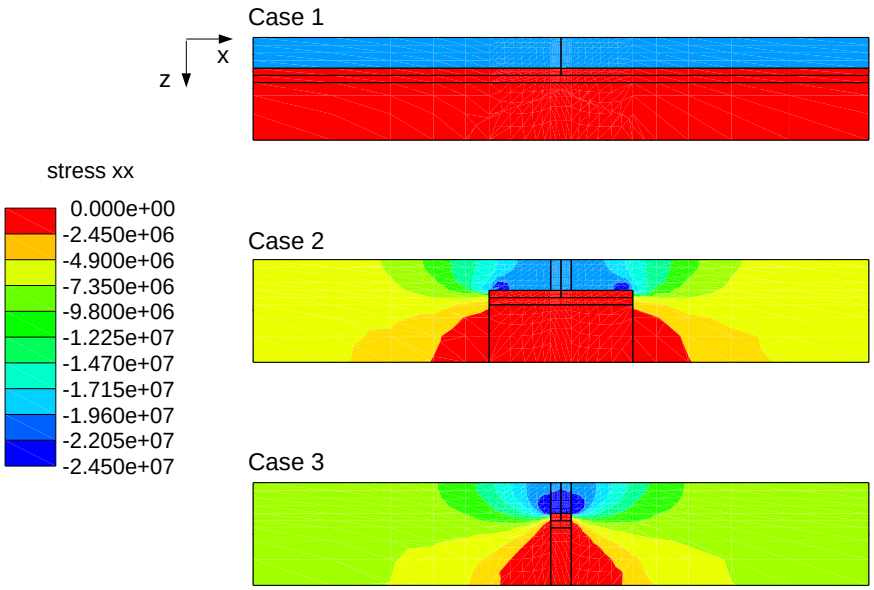

Plate 4. Cross sections of normal stress contours for the three model cases. The compression causes negative normal stresses, so, blue relates to high stress and red relates to zero stress. The scale is in megapascals. The concentration of stresses over the finite width shear zones is clearly evident, and the half-space approximation model shows a constant normal stress.

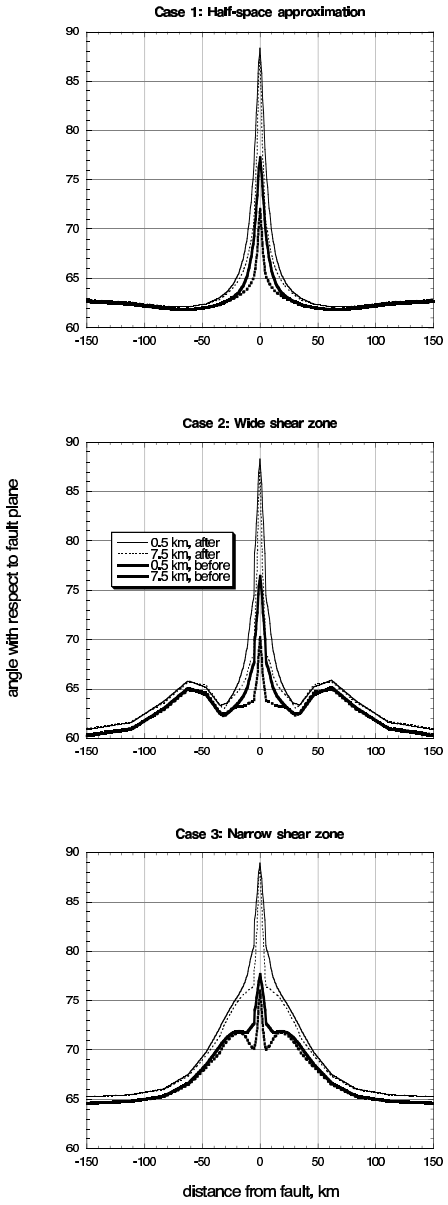

Figure 3. Maximum compressive stress orientation relative to the fault at 0.5 km (solid lines) and 7.5 km (dashed lines) depth versus distance from the fault for the three model cases. Narrow lines show the orientations immediately after an earthquake, and the heavier lines show the same immediately before an earthquake. Orientations at the fault are 90° to the fault after the earthquake and around 70° to 75° before the earthquake. Away from the fault, orientations are closer to 60° with some variations near the shear zone boundaries in cases 2 and 3.

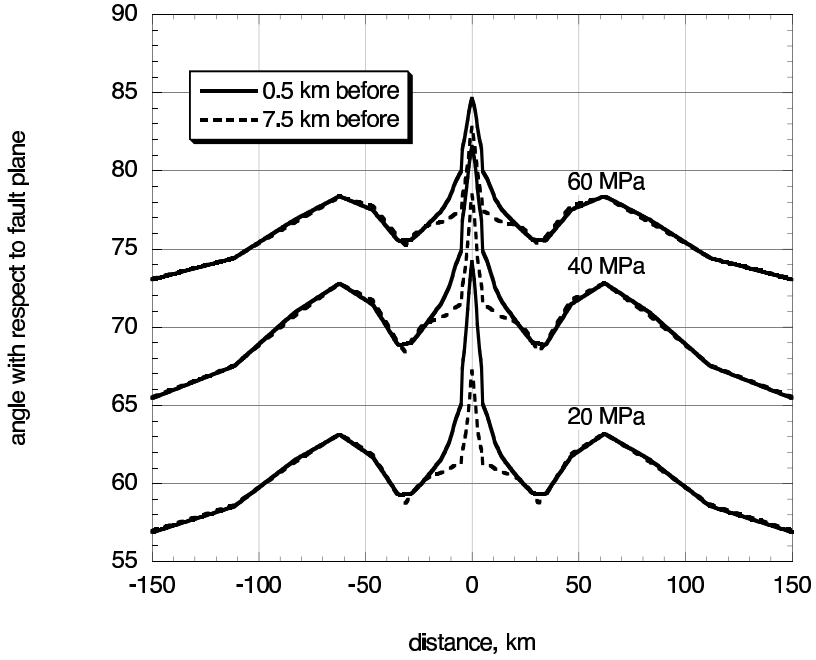

Figure 4. Maximum compressive stress orientation at 0.5 km (solid lines) and 7.5 km (dashed lines) depth versus distance from the fault for three possible normal stress calculations in the wide shear zone model. All results are shown for the preearthquake time step only. Choosing different amounts of compression moves the orientation angles up or down but does not change the overall variation as a function of distance from the fault.

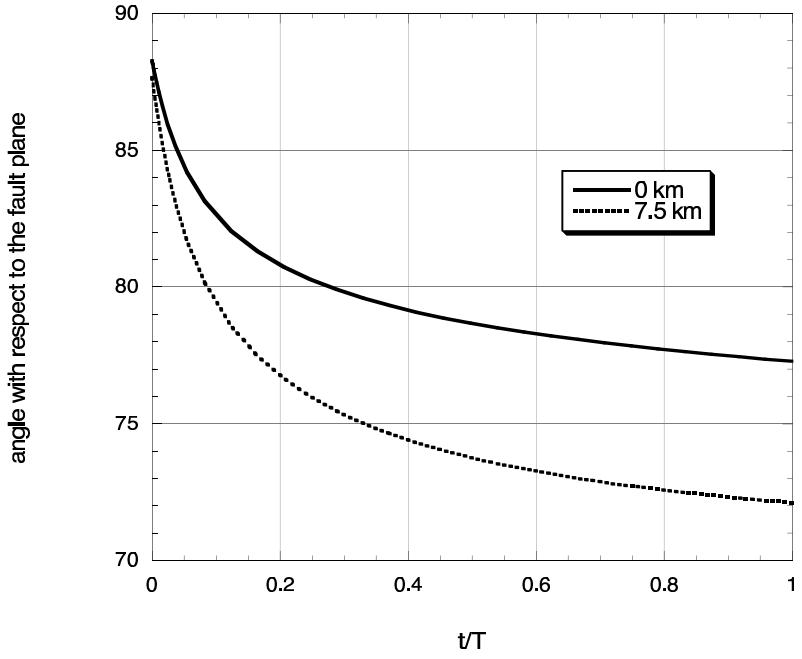

Figure 5. Maximum compressive stress orientation at 0.5 km (solid lines) and 7.5 km (dashed lines) depth versus time for nodes at the fault. The majority of the postseismic effect takes place in the first 20% of the earthquake cycle, or after ~10 Maxwell relaxation times (τ = 4.23 years, T = 250 years).

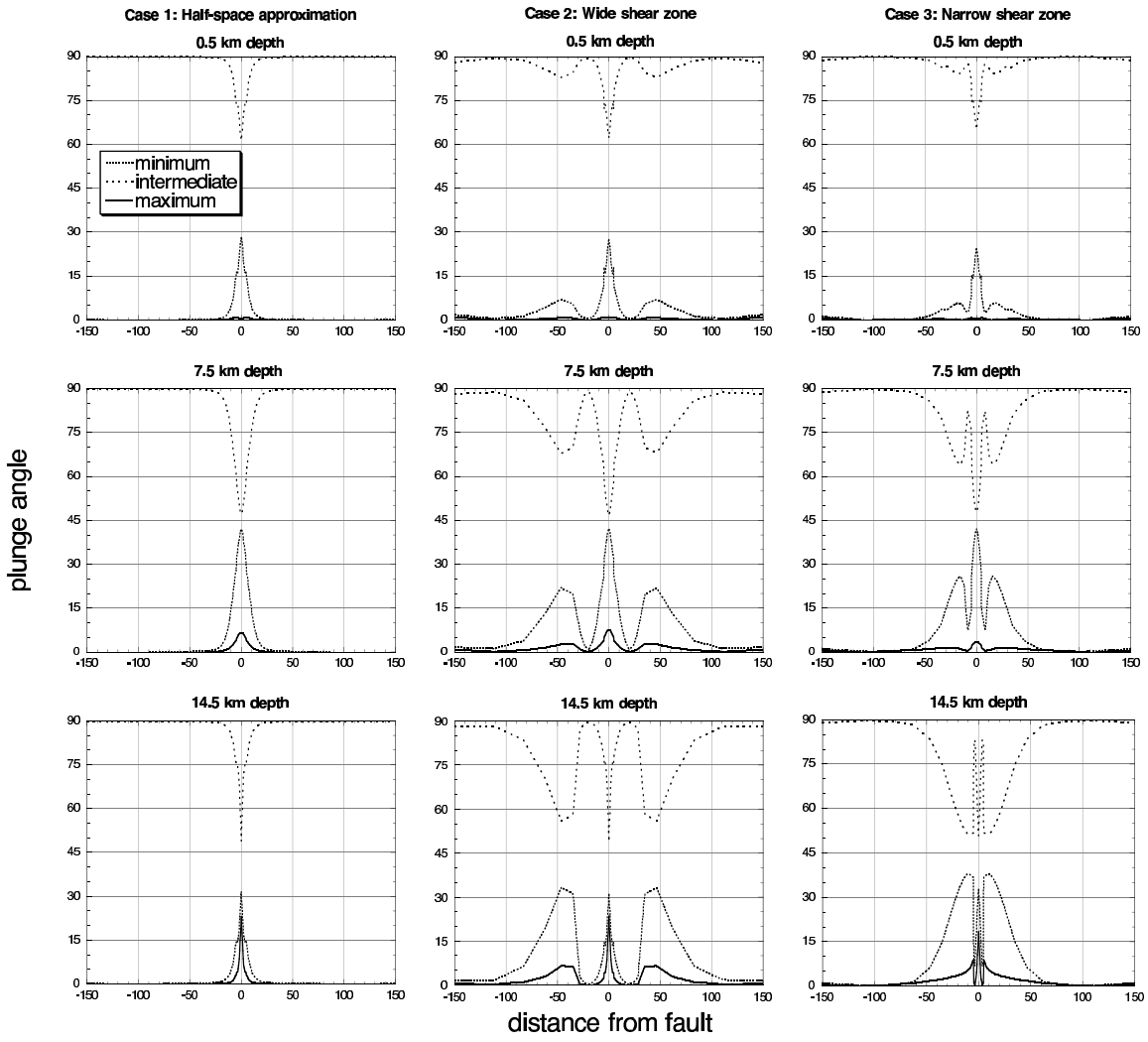

Figure 6. Plunge angles of the principal stress axes. Each column shows the results from each of the models, and the three rows are for depths of 0.5, 7.5, and 14.5 km. The maximum compressive stress is shown in the solid line, the intermediate in the sparsely dashed line, and the minimum in the densely dashed line. Results are plotted for the preearthquake time step only. The plunge angles are aligned in Andersonian fashion at the Earth's surface, with two principal axes in the horizontal plane and one perpendicular to it (deviation from this orientation near the fault is discussed in section 4.2 and Figure 11). The interface between the elastic upper crust and viscoelastic lower crust also acts as a near free surface, resulting in Andersonian alignment above the shear zones at 14.5 km depth.

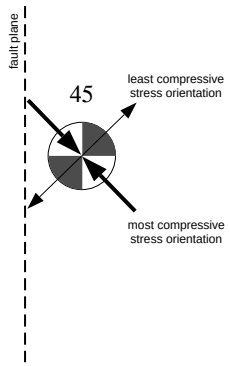

Figure 7. An example of the shear stress beach ball. The most compressive stress axis bisects the unshaded portion of the beach ball, the least compressive axis bisects the shaded portion, and the intermediate axis lies along the intersection of the two nodal planes. The number printed above the beach ball is the orientation of the MCS with respect to the fault.

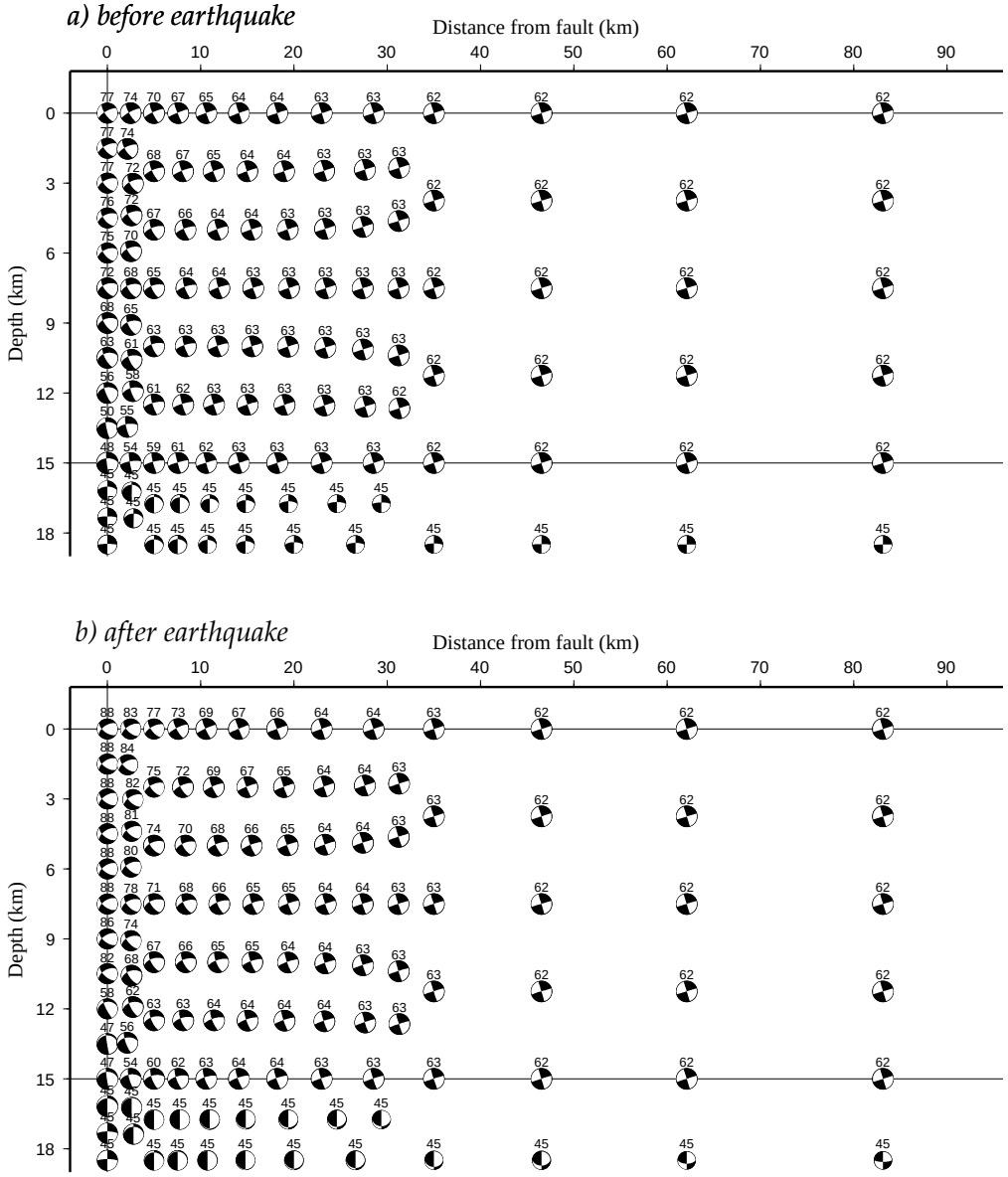

Figure 8. Shear stress beach balls for case 1, the half-space approximation model, (a) before and (b) after an earthquake. Plot only covers one half of the mesh and only out to a distance of 90 km from the fault. Numbers above each beach ball refer to the orientation of the maximum compressive stress with respect to the fault. The rotation of the principal stress axes away from their Andersonian orientation is clear near the fault. Also note the 45° orientation of the maximum compressive stress in the viscoelastic substrate (below 15 km), a result of the inability of the shear zone to retain normal stresses. When viewing the shear stress beach balls in Figures 8-10 and 13, keep in mind that while looking at a cross section through the mesh, the beach balls are plotted as though being viewed from map view.

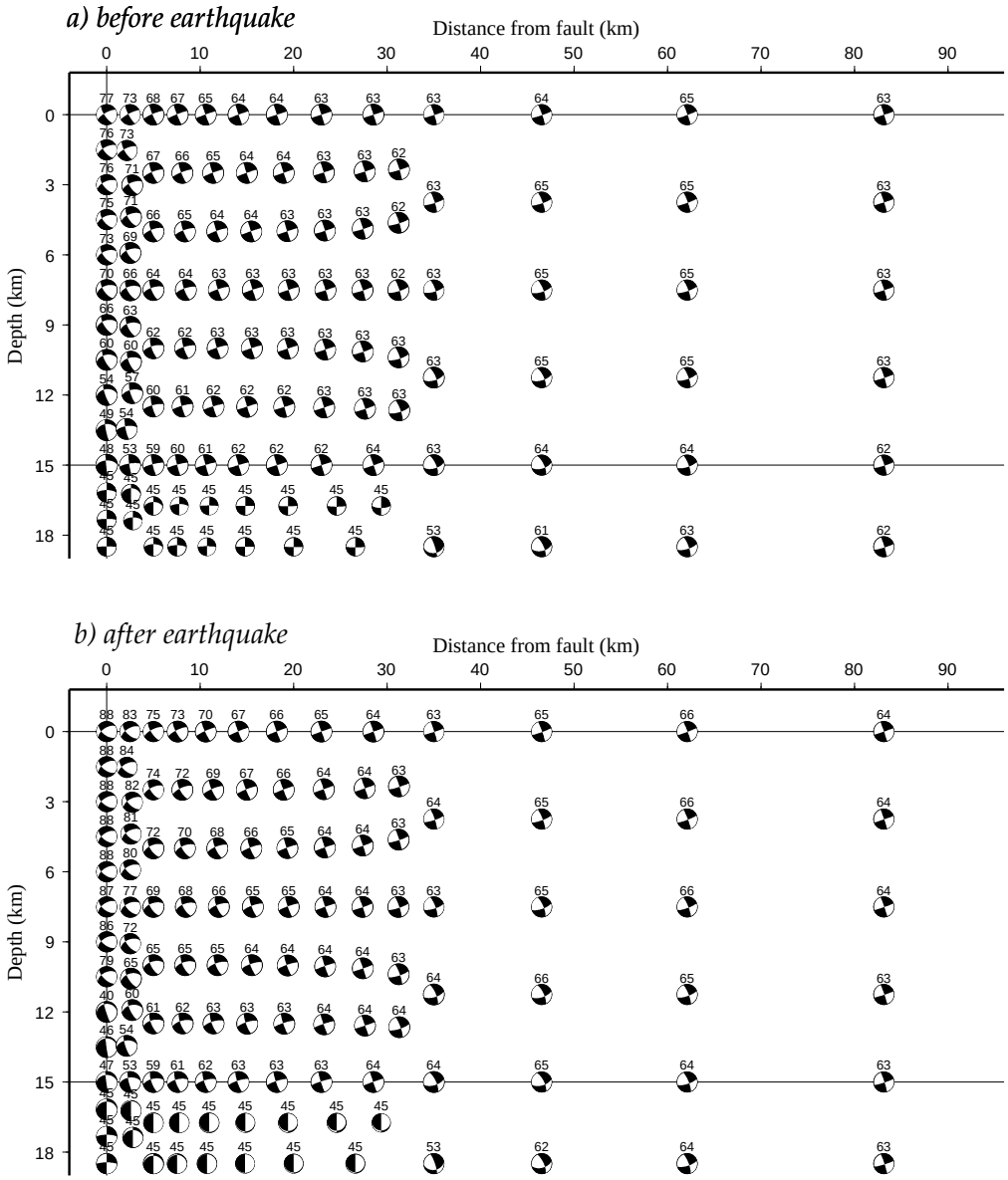

Figure 9. Shear stress beach balls for case 2, the wide shear zone model, (a) before and (b) after an earthquake. The rotation of the stress axes near the viscoelastic shear zone boundary (35 km from the fault) is clear between 10 and 15 km depth. See Figure 8 for further notes.

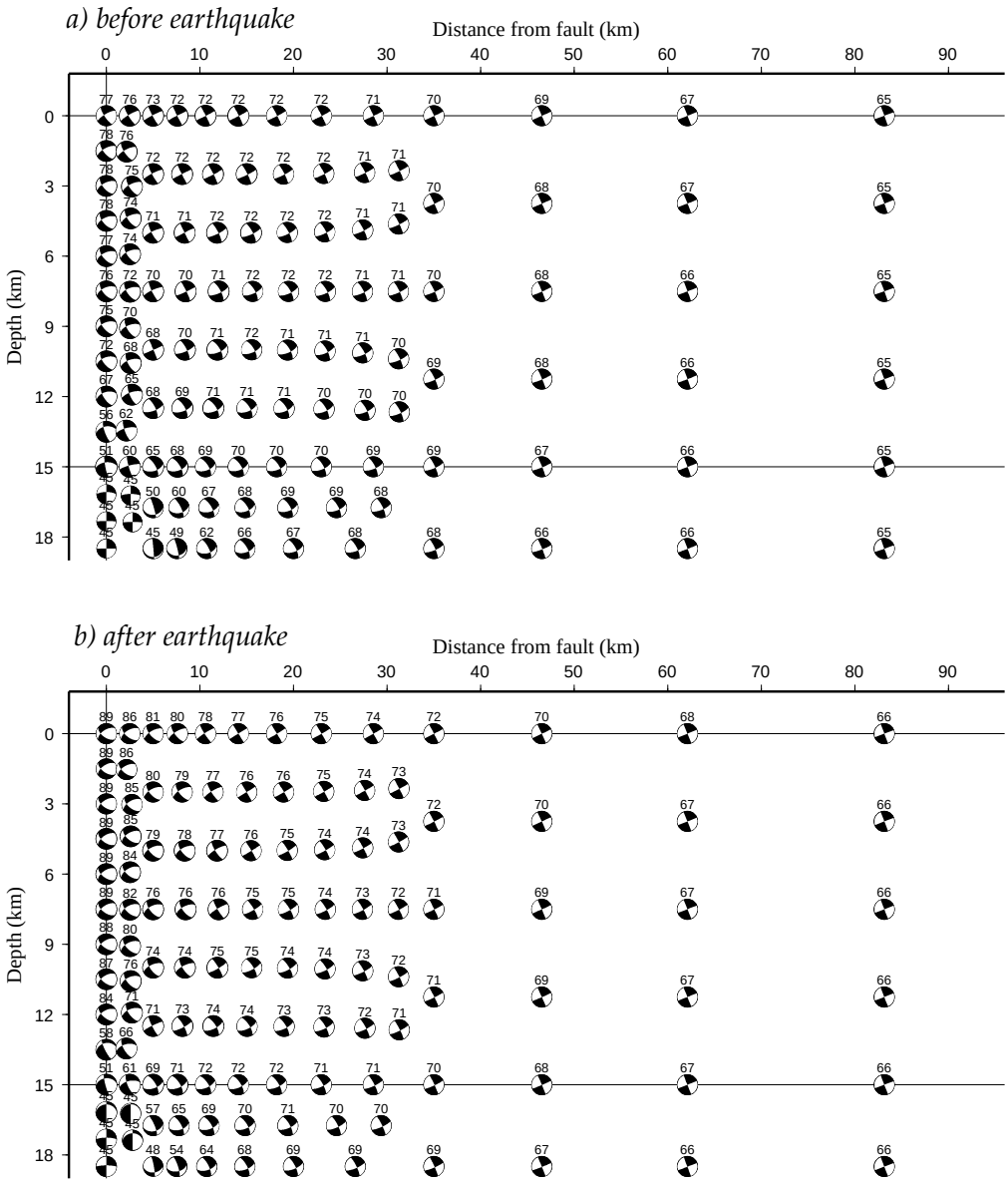

Figure 10. Shear stress beach balls for case 3, the narrow shear zone model, (a) before and (b) after an earthquake. See Figures 8 and 9 for notes.

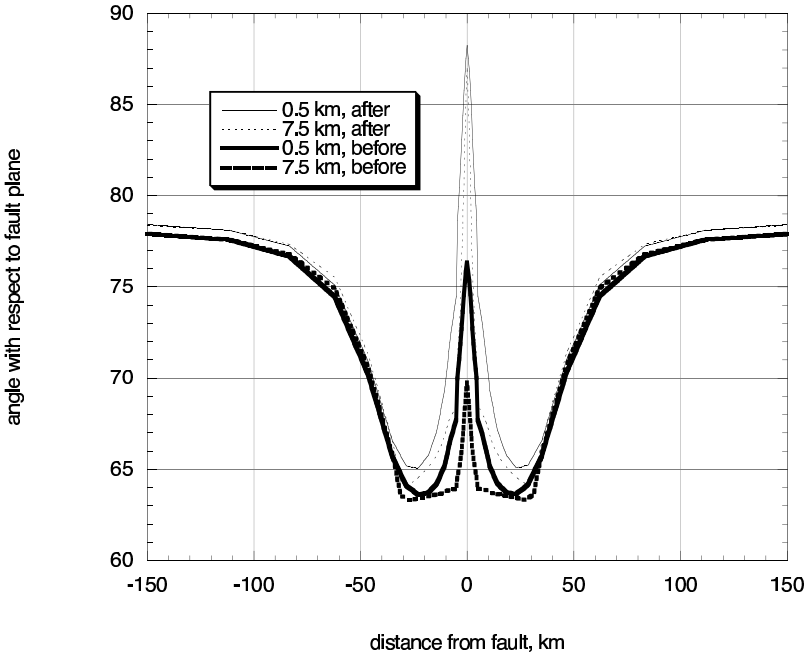

Figure 11. Maximum compressive stress orientation at 0.5 km (solid line) and 7.5 km (dashed line) versus distance from the fault for the wide shear zone case with a constant normal stress added, post hoc, to the shear stress calculation. Only the preearthquake results are shown. In this case, the orientation of the MCS is closer to being perpendicular to the fault in the far field, while similar to the orientations seen in Figure 3 near the fault.

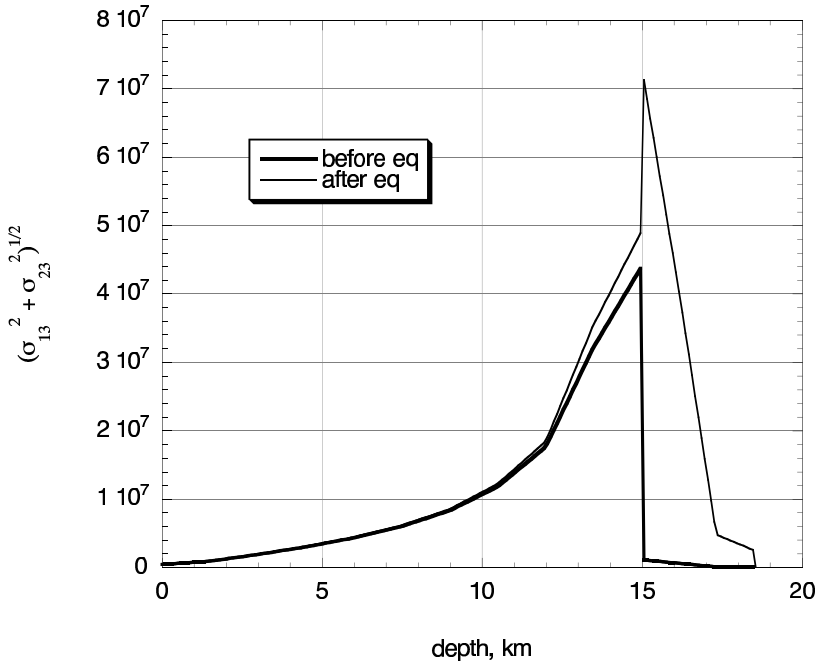

Figure 12. Horizontal shear stress ($\sqrt{\sigma_{xz}^2 + \sigma_{yz}^2}$) as a function of depth for the wide shear zone model. Results are taken from stresses on the fault, with the preearthquake time step shown in the thick line, and the postearthquake time step shown in the thin line. Horizontal shear stress approaches zero at the the free surface (0 km depth) and a maximum at 15 km depth. When the shear zone is relaxed (the preearthquake trace), horizontal shear stress approaches zero below 15 km depth. After the earthquake the horizontal shear stress is maximized in the shear zone.

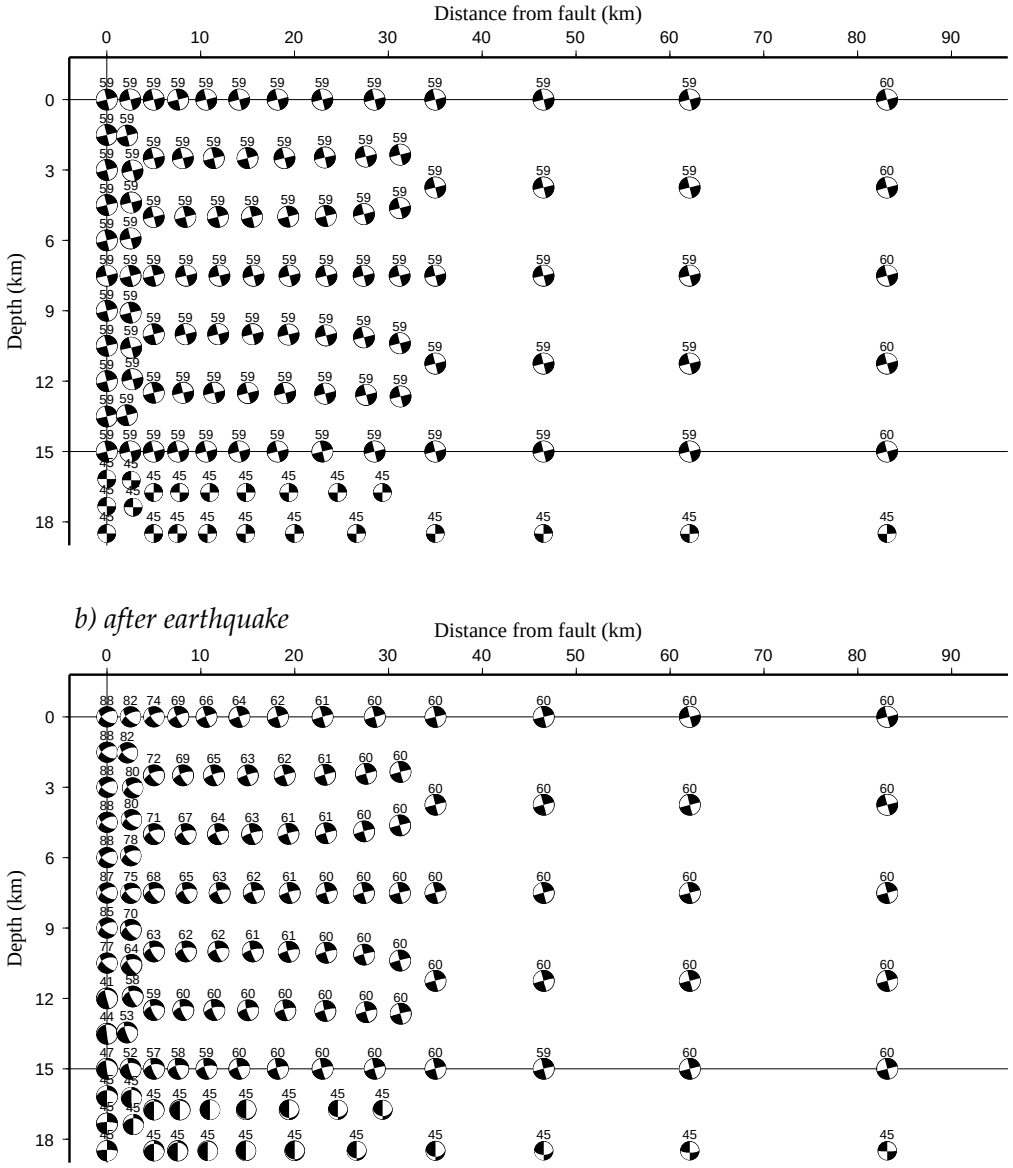

Figure 13. Shear stress beach balls for the first earthquake in the half-space approximation model (a) before and (b) after the earthquake. Before the first earthquake, stresses are uniform throughout the mesh, indicating simple shear.

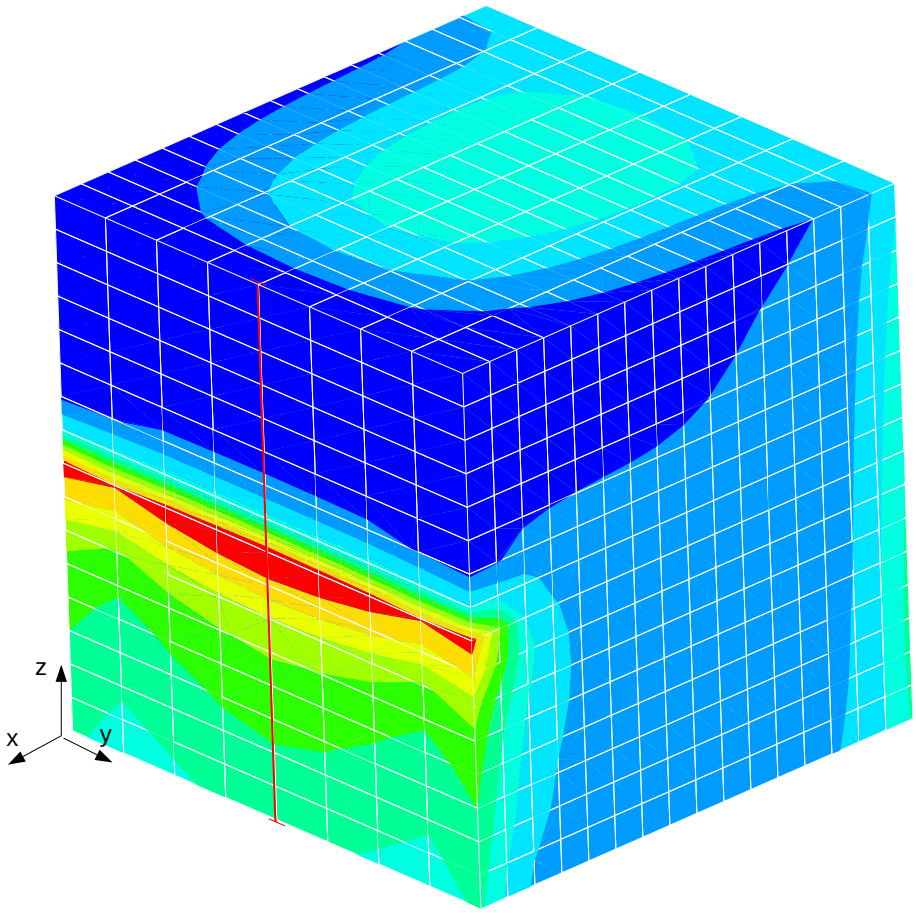

Plate 5. The mesh used for the resolution test. The dimensions of the mesh are 8x8x8, and this example has element dimensions of $\frac{1}{2}$x1x$\frac{1}{2}$, making the number of elements 16x8x16. Shown are contours of shear stress (σ_{xy}) for the resolution test problem. Also a red line shows the sampled nodes for the stress profile shown in Figure A1.

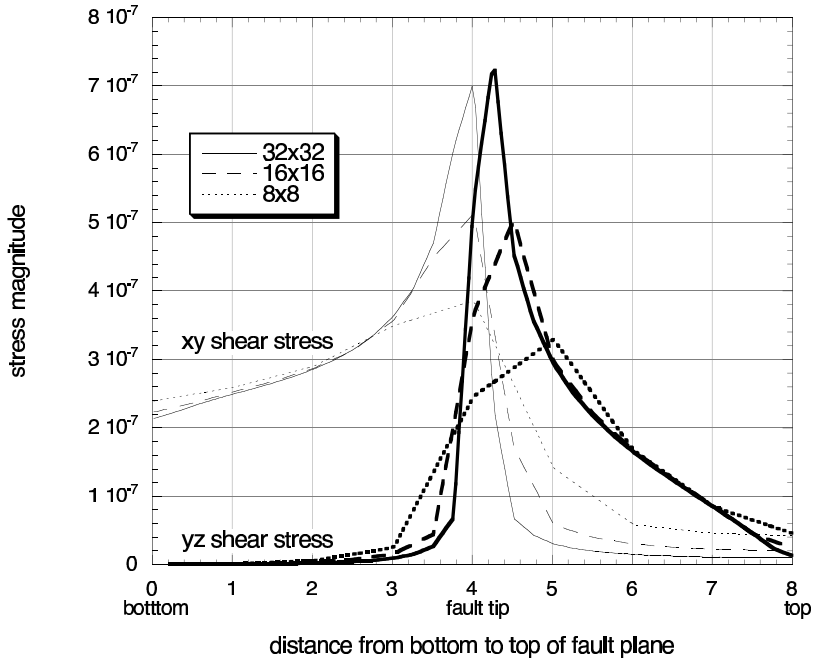

Figure A1. Stress profiles across the fault plane face of the cube used in the resolution test. The thin lines show σ_{xy}, and thick lines show σ_{yz}. The three different cases are shown with solid (32x32 case), dashed (16x16 case), and dotted (8x8 case) lines. While the 32x32 case certainly has the best resolution, it is clear that when the solution is examined more than two elements away from the fixed-face/free-face interface the three cases agree well.